Monthly Notices
of the
ROYAL ASTRONOMICAL SOCIETY

MNRAS **473,** 1359–1387 (2018)
Advance Access publication 2017 September 19

doi:10.1093/mnras/stx2414

Investigating the diversity of supernovae type Iax: a MUSE and NOT spectroscopic study of their environments

J. D. Lyman,[1]★ F. Taddia,[2] M. D. Stritzinger,[3] L. Galbany,[4] G. Leloudas,[5,6] J. P. Anderson,[7] J. J. Eldridge,[8] P. A. James,[9] T. Krühler,[10] A. J. Levan,[1] G. Pignata[11,12] and E. R. Stanway[1]

[1]*Department of Physics, University of Warwick, Coventry CV4 7AL, UK*
[2]*The Oskar Klein Centre, Department of Astronomy, Stockholm University, AlbaNova, SE-10691 Stockholm, Sweden*
[3]*Department of Physics and Astronomy, Aarhus University, Ny Munkegade 120, DK-8000 Aarhus C, Denmark*
[4]*PITT PACC, Department of Physics and Astronomy, University of Pittsburgh, Pittsburgh, PA 15260, USA*
[5]*Department of Particle Physics and Astrophysics, Weizmann Institute of Science, Rehovot 7610001, Israel*
[6]*Dark Cosmology Centre, Niels Bohr Institute, University of Copenhagen, Juliane Maries vej 30, DK-2100 Copenhagen, Denmark*
[7]*European Southern Observatory, Alonso de Córdova 3107, Casilla 19, Santiago 8320000, Chile*
[8]*Department of Physics, University of Auckland, Private Bag 92019, Auckland, New Zealand*
[9]*Astrophysics Research Institute, Liverpool John Moores University, IC2, Liverpool Science Park, 146 Brownlow Hill, Liverpool L3 5RF, UK*
[10]*Max-Planck-Institut für extraterrestrische Physik, Giessenbachstraße, D-85748 Garching, Germany*
[11]*Departamento de Ciencias Fisicas, Universidad Andres Bello, Avda. Republica 252, Santiago 8320000, Chile*
[12]*Millennium Institute of Astrophysics (MAS), Nuncio Monseñor Sótero Sanz 100, Providencia, Santiago 8320000, Chile*

Accepted 2017 September 12. Received 2017 August 19; in original form 2017 June 30

ABSTRACT

SN 2002cx-like Type Ia supernovae (also known as SNe Iax) represent one of the most numerous peculiar SN classes. They differ from normal SNe Ia by having fainter peak magnitudes, faster decline rates and lower photospheric velocities, displaying a wide diversity in these properties. We present both integral-field and long-slit visual-wavelength spectroscopy of the host galaxies and explosion sites of SNe Iax to provide constraints on their progenitor formation scenarios. The SN Iax explosion-site metallicity distribution is similar to that of core-collapse SNe and metal poor compared to either normal SNe Ia or SN 1991T-like events. Fainter members, speculated to form distinctly from brighter SN Iax, are found at a range of metallicities, extending to very metal poor environments. Although the SN Iax explosion-sites' ages and star formation rates are comparatively older and less intense than the distribution of star-forming regions across their host galaxies, we confirm the presence of young stellar populations (SPs) at explosion environments for most SNe Iax, expanded here to a larger sample. Ages of the young SPs (several $\times$ 10^7 to 10^8 yr) are consistent with predictions for young thermonuclear and electron-capture SN progenitors. The lack of extremely young SPs at the explosion sites disfavours very massive progenitors such as Wolf–Rayet explosions with significant fallback. We find weak ionized gas in the only SN Iax host without obvious signs of star formation. The source of the ionization remains ambiguous but appears unlikely to be mainly due to young, massive stars.

Key words: supernovae: general.

1 INTRODUCTION

The relative homogeneity of Type Ia supernovae (SN Ia) has allowed them to serve as precise extragalactic distance indicators after the application of empirically derived relations for light-curve shape (Phillips 1993) and colour (Tripp 1998). The similarity among the vast majority of SNe Ia suggests a commonality among their progenitor stars and their explosion physics. SNe Ia are generally thought to be the complete disruption of Chandrasekhar-mass white dwarfs (WDs) which undergo a thermonuclear runaway process of explosive carbon and oxygen burning. Despite a large population of 'normal' SNe Ia, increasing numbers of apparently similar events, but with spectroscopic and light-curve peculiarities have been discovered. It is not clear whether such underluminous (e.g. Filippenko et al. 1992a; Leibundgut et al. 1993; Turatto et al. 1996) and overluminous (Filippenko et al. 1992b; Phillips et al. 1992; Ruiz-Lapuente et al. 1992; Howell et al. 2006) events represent

★ E-mail: J.D.Lyman@warwick.ac.uk

extreme extensions of the SN Ia progenitor model or are distinct in their progenitor stars and explosion mechanisms. One particular event, SN 2002cx, also appeared to fall into the category of SN Ia, following the traditional SN classification scheme (Filippenko 1997), but garnered the title of the 'most peculiar known' SN Ia (Li et al. 2003). With early spectral similarity to the overluminous SN 1991T-like events – consisting of conspicuous high-ionization spectral features associated with Fe II and Fe III – but being relatively faint at peak ($M_R \sim -17.7$ mag), SN 2002cx prompted the classification of other 'SN 2002cx-like events' (e.g. Jha et al. 2006; Narayan et al. 2011). A comprehensive study of all objects designated as SN 2002cx-like events (hereafter SNe Iax) was presented by Foley et al. (2013). The sample has since expanded and a recent review by Jha (2017) discusses the current status of SN Iax observations and theory.

The primary distinctions of SNe Iax from normal SNe Ia are fainter peak magnitudes, lower ejecta velocities, no secondary near-infrared maxima (with light curves peaking in optical before near-infrared, unlike normal SNe Ia), and late-time spectra that do not become fully nebular (see Jha et al. 2006; Foley et al. 2013, 2016, for more in-depth discussion). However, even within the events classified as members of this group there appears a large degree of diversity. The low ejecta velocities of SNe Iax (2000–8000 cf. 10 000–15 000 km s^{-1} for normal SNe Ia around peak) imply that their explosions are of significantly lower energies, and their faint peak magnitudes indicate production of smaller amounts of radioactive ^{56}Ni (0.003–0.27 cf. ∼0.4–1.0 $M_\odot$ for normal SN Ia; e.g. Stritzinger et al. 2006; Childress et al. 2015). One of the leading scenarios to explain SNe Iax is that they are deflagrations of Chandrasekhar mass WDs (e.g. Branch et al. 2004; Phillips et al. 2007; Jordan et al. 2012; Kromer et al. 2013) that have accreted helium-rich material from a companion star (Foley et al. 2009; Liu et al. 2015b). Due to the extension of SNe Iax to low explosion energies and inferred ejecta masses, there is indirect evidence that at least some fraction of these SNe could leave bound remnants. Such 'failed' deflagrations are favoured to explain relatively bright but low ejecta velocity events such as SN 2014ck (Tomasella et al. 2016).

Support for the helium-accreting WD scenario has come from direct progenitor constraints and environmental constraints. McCully et al. (2014a) present the detection of a blue source at the location of SN 2012Z that is similar to the Galactic helium nova V445 Pup and limits for SN 2014dt provided by Foley et al. (2015) are also consistent with a similar progenitor system. Liu et al. (2015c) suggest a hybrid CONe WD + He-star as the most favourable progenitor system for SN 2012Z. The delay time to explosion for WD+He-star systems has been investigated by Wang, Justham & Han (2013), Wang et al. (2014) and Liu et al. (2015b) who found a time-scale of ∼100 Myr, in good agreement with observational constraints on their ages. Lyman et al. (2013) found that SN Iax host galaxy types closely match one drawn from the star formation (SF) rate density of the local Universe and the environments of SNe Iax trace the SF of their hosts at a similar level to core-collapse SNe II with expected delay times of tens of hundreds of Myr. This statistical estimate of their environment ages was backed up through analyses of the local stellar populations (SPs) of SNe 2008ha (Foley et al. 2014) and 2012Z (McCully et al. 2014a), which found environments harbouring young SPs with ages of 10–80 Myr.

Consistent with their young environments, it has also been suggested that some SNe Iax may be due to the collapse of massive stars. One particular example that has drawn attention is SN 2008ha. This was an extremely weak SN, even in comparison to other SN Iax, producing 0.003 $M_\odot$ of ^{56}Ni and possibly ejecting only a few tenths $M_\odot$ of material (Foley et al. 2009; Valenti et al. 2009), although it is not alone in this regard (e.g. SN 2010ae; Stritzinger et al. 2014). Massive star models explored to explain these very low energy and luminosity events include the collapse of very massive Wolf–Rayet (WR) stars with significant fallback on to a nascent black hole (Valenti et al. 2009; Moriya et al. 2010) and stripped-envelope electron-capture (SE-EC) SNe (Pumo et al. 2009; Moriya & Eldridge 2016). The scenario of very low luminosity SNe accompanying massive stellar collapse may be appealing to explain apparently SN-less gamma-ray bursts (GRBs; e.g. Della Valle et al. 2006; Fynbo et al. 2006; Michałowski et al. 2016), if indeed they are related to other long-duration GRBs (LGRBs), and thus a result of the collapse of massive stars (see e.g. Gal-Yam et al. 2006; Gehrels et al. 2006).

Adding further diversity to the sample, we note that for one event, SN 2008ge, no evidence for a young SP at the explosion site, or within the S0 host galaxy, was found by Foley et al. (2010a). Furthermore, for two events, SNe 2004cs and 2007J, helium (and potentially hydrogen) was detected in their spectra. Doubt as to their validity as SNe Iax members has been raised by White et al. (2015), who classify them instead as core-collapse Type IIb SNe, although this was refuted by Foley et al. (2016).

It is apparent that the group of SNe that have been labelled SN Iax is a heterogeneous group with many outliers (e.g. Tomasella et al. 2016), and multiple progenitor systems and explosion mechanisms could be responsible (Foley et al. 2013; Jha 2017). The sample has now grown to a size where statistical studies can elucidate further information on the progenitor systems, beyond characterizing individual examples. Environmental diagnostics have played a central role in the understanding of other well-known transient types (see Anderson et al. 2015, and references therein) and, in particular, the Multi-Unit Spectroscopic Explorer (MUSE; Bacon et al. 2010) instrument mounted at the Very Large Telescope (VLT) is revolutionizing the way such studies are performed. MUSE is an integral field spectrograph (IFS) providing spatial and spectral information at the transient explosion site and across the host galaxy system in a single pointing (e.g. Galbany et al. 2016a; Prieto et al. 2016; Izzo et al. 2017; Krühler et al. 2017).

In this paper, we perform spectroscopic environmental measurements for a large number of SNe Iax using both IFS and long-slit data from VLT/MUSE and Nordic Optical Telescope/Andalucia Faint Object Spectrograph and Camera (NOT/ALFOSC), thereby providing additional constraints on the nature of the progenitor systems and investigating whether their wide-ranging explosion characteristics are matched by large spreads in environmental measures. In Section 2, we present our observations. Our methods for the MUSE-observed sample are given in Section 3 and in Section 4 we highlight similarities and differences for our NOT-observed sample's analysis. Results are presented and discussed in Sections 5 and 6, respectively. Throughout the paper, we use $\log(\mathrm{O/H}) + 12 = 8.69$ dex as the solar abundance (Asplund et al. 2009) and adopt the cosmological parameters $H_0 = 73.24$ km s^{-1} Mpc^{-1} (Riess et al. 2016) and $\Omega_\mathrm{m} = 0.3$.

2 OBSERVATIONS AND DATA REDUCTION

The current number of SN Iax discovered is around 50 events (Jha 2017). Our sample consists of 37 SNe Iax host galaxies observed with VLT/MUSE or NOT/ALFOSC. The hosts span a redshift range of 0.004–0.08. Membership of our sample as SN Iax up to SN 2012Z is presented in Foley et al. (2013). Additionally, we add SN 2013dh (Jha et al. 2013), SN 2013en (Liu et al. 2015a), SN

Table 1. Observations of SN Iax host galaxies with VLT/MUSE.

SN name	Host galaxy	z	R_{25} (arcsec)	Date Obs.	Exp. time (s)	Seeing (arcsec)
1991bj	IC 344	0.018	14.4	2015 September	4×700^a	1.7
2002bp	UGC 6332	0.021	36.9	2015 April	4×555	1.2
2002cx	CGCG 044-035	0.024	20.8	2016 January	4×700^a	1.7
2004cs	UGC 11001	0.014	38.7	2016 March	4×555	1.1
2005P	NGC 5468	0.009	78.9	2016 January	4×555	1.0
2005hk	UGC 272	0.013	43.4	2015 October	4×555	1.4
2008ae	IC 577	0.030	15.8	2015 November	4×700^a	0.9
2008ge	NGC 1527	0.004	111.5	2015 September	4×555	0.6
2008ha	UGC 12682	0.005	40.5	2015 November	4×555	1.4
2009J	IC 2160	0.016	61.3	2015 September	4×555	2.0
2010ae	ESO 162-017	0.004	61.3	2015 September	4×700^a	1.8
2010el	NGC 1566	0.005	249.6	2015 September	4×520	1.5
2011ce	NGC 6708	0.009	34.5	2015 September	4×555	0.9
2012Z	NGC 1309	0.007	65.7	2015 October	4×555	0.5
2013gr	ESO 114-007	0.007	54.6	2015 September	4×555	1.8
2014dt	NGC 4303	0.005	193.7	2016 January	4×520	1.9
2014ey	CGCG 048-099	0.032	19.8	2016 February/March^b	5×700^a	0.7
2015H	NGC 3464	0.012	77.1	2015 December	4×555	1.1

Notes. [a]Sky subtraction was done using blank regions of on-source exposures.
[b]The best five exposures from two incomplete observing attempts were combined.

2013gr (Hsiao et al. 2013), SN 2014ey (Goobar 2017; Carnegie Supernova Project, in preparation), SN 2014ck (Tomasella et al. 2016), SN 2014dt (Ochner et al. 2014), SN 2015H (Magee et al. 2016), PS 15aic (Pan et al. 2015), PS 15csd (Harmanen et al. 2015), SN 2015ce (Balam & Graham 2015) and SN 2016ado (Tonry et al. 2016). Here, we detail the observations taken for our sample on the two instruments.

2.1 VLT/MUSE

Observations of the host galaxies were carried out in a MUSE programme running between 2015 September and 2016 March apart from the host of SN 2002bp, which was observed as part of an earlier programme (as this galaxy has also hosted other SNe) in 2015 April. The time lag between the SN and our observations is more than 2 yr for all but two events, SNe 2014dt and 2015H. In both these cases, it is possible to identify broad forbidden line emission arising from the SN ejecta (see Foley et al. 2016 for an overview of SN Iax late-time spectra). These are analysed further in Appendix A where the late-time SN spectra and any impact on our environmental analyses are presented. In essence, we do not consider the presence of faint underlying signal from these hydrogen-poor, non-interacting events to significantly impact our emission-line-based environmental analyses.

The strategies for sky subtraction with MUSE depended on the angular size of each host galaxy. For galaxies that did not cover the field of view of MUSE, blank sky spaxels within the on-source exposures could be used to create the sky spectrum to subtract. Otherwise, we included two off-source shorter exposures of nearby blank sky interspersed among the on-source exposures. Four on-source exposures, rotated 90 deg from each other, were used in each case to account for detector artefacts. The details of the exposures taken are given in Table 1. The seeing values were determined by the full width at half-maximum (FWHM) of a point source in the (spectrally) flattened data cubes, in the absence of a suitable source we used the observatory's estimate of the conditions provided in the headers. All data were reduced and combined using version 1.6.2 of the ESO MUSE pipeline via REFLEX (Freudling et al. 2013) with default parameters. The ESO MUSE pipeline employs an empirical method for the removal of the sky signal; however, this can leave significant residuals, particularly in the redder part of the spectrum where sky lines are prominent. To combat this, Zurich Atmospheric Purge (ZAP;[1] Soto et al. 2016) has been developed. We additionally applied this method to our already reduced data cubes to correct these residuals. Where we took off-source sky exposures, we applied ZAP to the reduced off-source blank-sky exposures, before applying the results to the on-source combined data cubes. For those hosts that did not fill the field of view of MUSE, the correction to be applied by ZAP was calculated using blank regions of the on-source data cubes. Although some residuals were still present, they were significantly reduced compared to the standard sky-subtraction method.

2.2 NOT/ALFOSC

We observed 21 host galaxies of SNe Iax at the NOT using ALFOSC over two campaigns during 2016 March, September and 2017 April. The data were reduced largely following the same procedures described in Taddia et al. (2013, 2015b), which we additionally describe here.

We obtained long-exposure ($\gtrsim$1800 s), long-slit spectra of the H II regions within the host galaxies, by placing the slit at the SN position and choosing a position angle such that the galaxy centre or other bright H II regions near the SN location were captured. In most cases, the slit contained a few H II regions bright enough for our analysis. For all but SN 2008A, the slit was positioned to go through the host galaxy nucleus. The host of SN 2008A is fairly edge on (and the nucleus is subsequently extinguished) with diffuse SF (Lyman et al. 2013; McCully et al. 2014b). As such, we opted to align the slit through a reasonably bright H II region in order to increase our chances of obtaining metallicity constraints for the host. The instrumental set-up chosen was the same as adopted for the study presented in Taddia et al. (2013, 2015a), i.e. ALFOSC with grism #4 (wide wavelength range ~3500–9000 Å) and a 1

[1] http://muse-vlt.eu/science/tools

Table 2. Observations of SN Iax host galaxies with NOT/ALFOSC.

SN name	Host galaxy	z	R_{25} (arcsec)	Date Obs.	Exp. time (s)	Seeing (arcsec)
1999ax	SDSS J140358.27+155101.2	0.023[a]	–	2016 March	1200 × 3	0.8
2002cx	CGCG 044-035	0.024	20.8	2016 March	1200 × 3	1.1
2003gq	NGC 7407	0.021	59.9	2016 September	1800 × 3	0.8
2004gw	CGCG 283-003	0.017	38.8	2016 March	1200 × 3	1.1
2005cc	NGC 5383	0.008	94.9	2016 March	1800 × 1	1.2
2006hn	UGC 6154	0.017	29.3	2016 March	1800 × 2	1.7
2007J	UGC 1778	0.017	36.1	2016 September	1800 × 3	1.3
2007qd	SDSS J020932.73−005959.8	0.043	25.1	2016 September	1800 × 3	1.0
2008A	NGC 634	0.016	62.7	2016 September	1800 × 3	0.7
2009ku	APMUKS(BJ) B032747.73-281526.1	0.079	–	2016 September	1800 × 3	1.7
2011ay	NGC 2315	0.021	40.5	2016 March	1200 × 3	1.0
PS1-12bwh	CGCG 205-021	0.023	23.8	2017 April	1800 × 3	1.1
2013dh	NGC 5936	0.013	43.4	2016 March	1200 × 3	1.6
2013en	UGC 11369	0.012	34.5	2016 March	1200 × 2	1.5
2014ck	UGC 12182	0.005	38.8	2016 March	1800 × 1	1.7
2014ek	UGC 12850	0.023	28.7	2016 September	1800 × 3	1.0
2015H	NGC 3464	0.012	77.1	2016 March	1200 × 3	1.3
2015ce	UGC 12156	0.017	28.7	2016 September	1800 × 3	1.0
PS 15aic	SDSS J133047.95+380645.0	0.056	22.3	2016 March	1800 × 2	1.2
PS 15csd	SDSS J020455.52+184815.0	0.044[b]	–	2016 September	1800 × 3	0.7
2016ado	SDSS J020305.81−035024.5	0.043	–	2016 September	1800 × 3	1.3

Notes. [a]An adjacent galaxy is present at $z = 0.059$ (as measured from Hα in the NOT spectrum).
[b]Redshift from Hα emission of host galaxy in PESSTO classification spectrum.

arcsec wide slit, resulting in an FWHM spectral resolution of ∼16–17 Å. Details of the observations and exposure times adopted for each host galaxy observation are listed in Table 2.

First, the 2D (dimensional) spectra were bias subtracted and flat-field corrected in a standard way. When available, multiple exposures were then median-combined to remove any spikes produced by cosmic rays. Otherwise, we removed them using the L.A.Cosmic removal algorithm (van Dokkum 2001).

We extracted the trace of the brightest object in the 2D spectrum (either the galaxy nucleus, a bright star or an H II region with a bright continuum) and fitted with a low-order polynomial. The precision of this trace was checked by plotting it over the 2D spectrum. We then shifted the same trace in the spatial direction to match the position of each H II region visible in the 2D spectrum, and then extracted a 1D spectrum for each H II region. The extraction regions were chosen by looking at the Hα flux profile. The extracted spectra were wavelength and flux calibrated using an arc-lamp spectrum and a spectrophotometric standard star, observed on the same night or (in 2016 March) during the same week, respectively. Following Stanishev (2007), we removed the second-order contamination, which characterizes the spectra obtained with grism #4, from each spectrum. In this study, we included all the spectra showing at least Hα and [N II] λ6583 emission lines.

3 MUSE DATA ANALYSIS AND METHODS

To analyse the data cubes, we used IFUANAL,[2] a package developed in PYTHON to perform spaxel binning, stellar continuum and emission-line fitting of IFU data following work done by Stanishev et al. (2012) and Galbany et al. (2014). Further documentation is available for the package but we also detail the relevant analysis procedures in the following subsections.

The effects of Galactic reddening were removed for each cube using the extinction maps of Schlafly & Finkbeiner (2011) and adopting an $R = 3.1$ Cardelli, Clayton & Mathis (1989) reddening law before correcting to rest frame using redshifts for each host given by the NASA/IPAC Extragalactic Database (NED).[3]

3.1 Spaxel binning

As the spaxels in MUSE data are typically smaller than the seeing and typical sizes of objects of interest (i.e. H II regions), we utilized binning methods in order to combine the signal of adjacent physically related spaxels, as well as improve the SNR for faint regions. For every galaxy except NGC 1527 (the host of SN 2008ge), we adopted a binning method aimed at segmenting H II regions. For NGC 1527, we used the Voronoi binning method based on achieving a target SNR of the bins in the continuum. Additional to these algorithmically created bins, we manually added two custom bins, a fibre-like 2 arcsec bin on the host nucleus and a bin at the explosion site of the SN using the same radius limit as for our H II region binning (Section 3.1.1). For any cases where it was evident that foreground stars were affecting the binning algorithm, these were removed using a circular mask before repeating the binning. A single weighted-average spectrum was used to represent each bin, which was forwarded for stellar continuum and emission-line fitting. An overview of the binning performed for each data cube is given in Table 3.

3.1.1 H II *region binning*

In order to separate H II regions into bins, we use a method based on the HIIEXPLORER[4] algorithm (Sánchez et al. 2012b; Galbany

[2] https://github.com/Lyalpha/ifuanal

[3] http://ned.ipac.caltech.edu/

[4] http://www.caha.es/sanchez/HII_explorer/

Table 3. Details of spatial binning for the data cubes.

SN name	Binning algorithm[a]	N_{bins}	Survey fibre bin?	Explosion-site astrometry[b]
1991bj	H II region	31	Y	NTT/EMMI (R)
2002bp	H II region	67	Y	IAUC offsets
2002cx	H II region	17	Y	IAUC offsets
2004cs	H II region	90	Y	IAUC offsets
2005P	H II region	127	N	Swope/SITe3 (*r*)
2005hk	H II region	87	Y	VLT/FORS1 (R)
2008ae	H II region	58	Y	Swope/SITe3 (*r*)
2008ge	Continuum	10237	Y	Gemini/GMOS-S (*r*)
2008ha	H II region	50	Y	Swope/SITe3 (*r*)
2009J	H II region	61	Y	Swope/SITe3 (*r*)
2010ae	H II region	39	Y	NTT/EFOSC (R)
2010el	H II region	88	Y	NTT/EFOSC (R)
2011ce	H II region	182	Y	NTT/EFOSC (R)
2012Z	H II region	311	Y	Swope/SITe3 (*r*)
2013gr	H II region	48	Y	NTT/EFOSC (V)
2014dt	H II region	109	N	SOAR/Goodman (clear)
2014ey	H II region	95	Y	Swope/SITe3 (*r*)
2015H	H II region	148	Y	NTT/EFOSC (V)

Notes. [a]The H II region and continuum binning are described in Sections 3.1.1 and 3.1.2, respectively. [b]If an image of the SN was used to astrometrically align the MUSE cube, the telescope/instrument (filter) is given. Otherwise offsets from the host given in the discovery IAU Circular were used.

et al. 2016a). A narrow 30 Å filter was simulated in the data cubes, centred on the Hα emission line, and from this we subtracted a continuum level determined by interpolation of the flux in two simulated neighbouring continuum filters. From the Hα map, a region of blank sky was used to determine the background median and standard deviation. Seeds of potential bins were found as all peaks in the flux distribution that were $>8\sigma$ above the background median. The Hα map was smoothed with a narrow Gaussian before the peak detection algorithm was run to avoid finding spurious peaks due to noise fluctuations. Seeds were ordered in descending Hα flux and, starting with the brightest seed, every pixel in the Hα map that satisfied the following conditions was added to the candidate bin:

(i) within 250 pc (or 1/2 × FWHM of the MUSE cube if this was larger) of the seed pixel;
(ii) a flux at least 10 per cent of the seed pixel flux;
(iii) $>5\sigma$ above the background median.

If the pixels satisfying these conditions were a contiguous group of eight or more, then the bin was stored, otherwise the bin was rejected. The next seed (that had not already been assigned a bin) was then used. This process was repeated until all seeds were used.

The nature of the HIIEXPLORER algorithm means that bins in bright areas of the galaxy are grown to a similar size (i.e. the maximum radius specified). Our limit is conservative in comparison to observed sizes of H II regions; however, our choice was driven by the approximate mode of H II region sizes (e.g. Oey et al. 2003). Thus, although we will crop any giant regions that can have diameters up to ∼1 kpc, our limit means the majority of bins are representative of H II region sizes. As shown in the top panels of Fig. 1, the algorithm captures each of the individual regions above our flux limit, although some of the diffuse emission and the outer extents of very large complexes may be missed.

The typical minimum flux in the Hα narrow-band image we consider as a bin seed was a few × 10^{-18} erg s^{-1} cm^{-2} Å^{-1}. The number of bins found by the algorithm for each galaxy is shown in Table 3.

3.1.2 *Continuum binning*

NGC 1527 is a smooth-profiled, early-type S0 galaxy (Foley et al. 2010a) and as such we chose another method of binning the spaxels. Specifically, we adopted the Voronoi binning method of Cappellari & Copin (2003), designed to attain a minimum signal to noise in the continuum (5590–5680 Å) for each bin whilst maximizing spatial resolution. Individual spaxels were required to have a signal-to-noise ratio (SNR) of 3 in the continuum window and these were binned by the algorithm to a target of SNR = 40 per bin. In practice, individual spaxels in the central ∼2 kpc of the galaxy had SNR $\gtrsim$ 40 and so these were not binned. Even with the reasonably high SNR target, bin sizes only reached radii of ∼100–150 pc in the outskirts of the field of view.

3.1.3 *Host nucleus bins*

For each MUSE cube where the central nucleus of the host galaxy was in the field of view, we simulated a representative survey fibre by creating a 2 arcsec diameter bin centred on the nucleus. The results pertaining to these bins will be referred to as 'nucleus' values.

3.1.4 *SN explosion-site bins*

We manually added a bin at the location of the SN explosion site in each host. The explosion-site bins were circular with a diameter equal to that used for the H II region binning (Section 3.1.1). The location was found via astrometric alignment of an SN discovery image or, if no image could be obtained, we used offsets from the host centre given in discovery IAU circulars (the method used for each is given in Table 3). Where a suitable image was found, the data cube was convolved with a filter transmission matching the SN image filter to create a MUSE image. The MUSE field

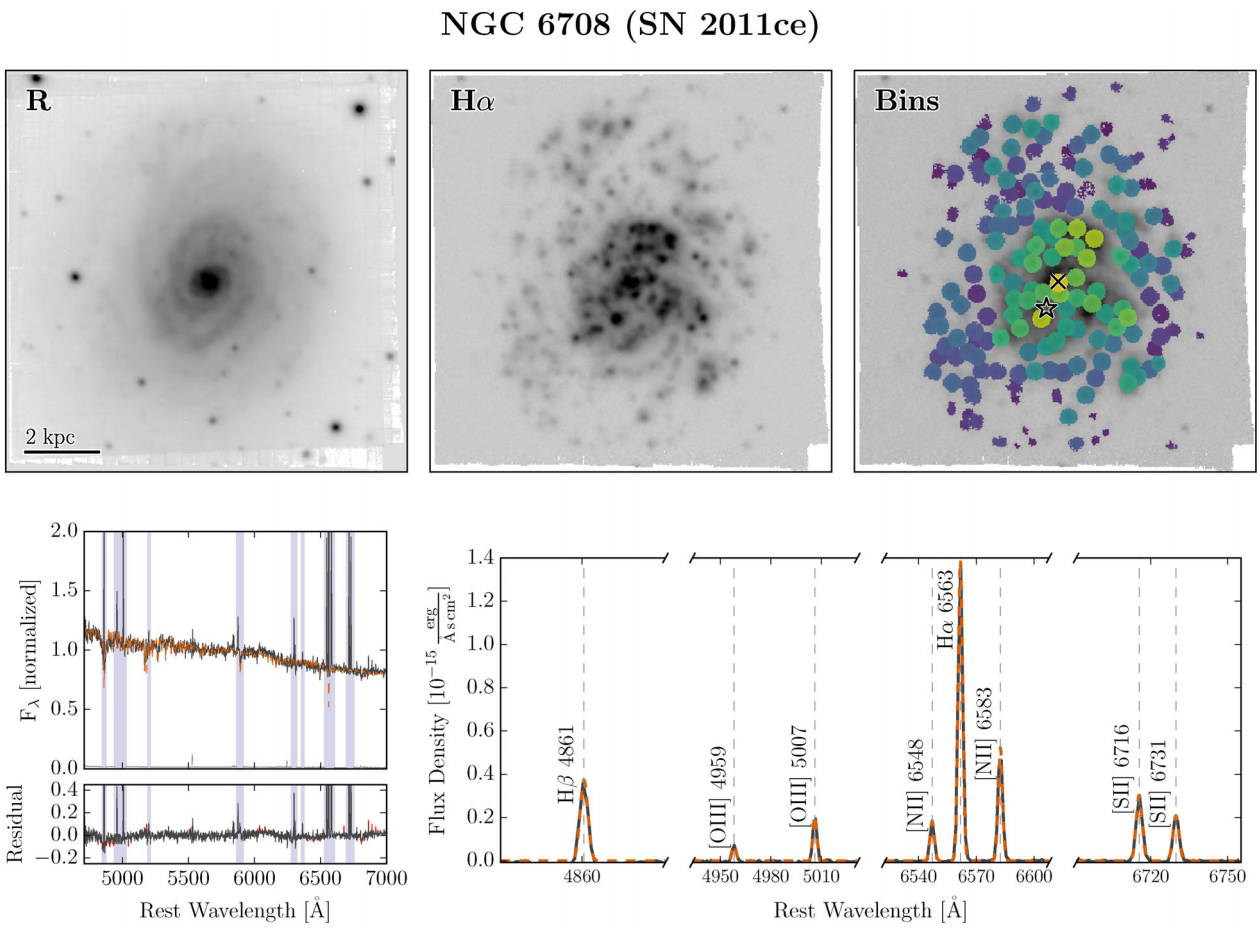

Figure 1. An example of the binning and fitting routines performed on each data cube described in Sections 3.1–3.3, as shown for NGC 6708 (the host of SN 2011ce). *Top:* the spectral axis has been convolved with the transmission profile of the appropriate filter to produce an *R*-band *(left)* and H α *(middle)* image of the MUSE cube; north is up, east is left. The bins that were produced by the binning algorithm (Section 3.1.1) are shown (arbitrarily coloured based on their H α brightness) overlaid by the location of the nucleus and the SN explosion site, given by black $\times$ and 'star' symbols, respectively *(right)*. *Bottom:* the continuum fitting of an example spectrum *(left)*. Black shows the observed spectrum and orange the STARLIGHT fit. Regions around strong emission lines were masked and these are shown as vertical shaded regions. Red elements in the residual plot are those flagged as bad pixels or clipped by STARLIGHT. The continuum fits were subtracted from the spectra before emission-line fitting *(right)*. Orange dashed line shows the multiple Gaussian fit over the observed residual emission spectrum – line identifications for the main lines used in our analysis are shown.

of view is comparatively small at $\sim$1 arcmin and so, generally, only a small number of common sources with which to tie the astrometric alignment were present. We therefore first registered the SN and MUSE images with their WCS information before fitting a transformation that allowed a shift only.

Two of our MUSE images detected their respective SN at late times – SN 2014dt and SN 2015H, and we used these as a test of our alignment procedures. With three sources to tie the fit, our transformed location of SN 2015H was 0.6 pixels (0.12 arcsec) offset from the centroid location of the SN in the MUSE image itself. For SN 2014dt, the MUSE image is quite poor seeing and we are limited to using diffuse H II regions as common sources; nevertheless, we find our transformed location to be only 1 pixel offset from the centroid of the SN. When compared to the typical sizes of the explosion-site bins, uncertainties in the alignment of $\sim$1 pixel do not significantly impact our results.

3.2 Stellar continuum fitting

Although our analysis of the underlying stellar continuum is restricted as our regions of interest are emission dominated, and generally without sufficient signal in the continuum to permit a robust analysis from the fitting of absorption indices, we nevertheless must account for the continuum in order to determine accurate emission-line results. In order to fit the stellar continuum, we used the spectral synthesis package STARLIGHT (Cid Fernandes et al. 2005). A minimization of the (model $-$ data) residuals is performed by summing contributions of single stellar populations (SSPs) after masking regions dominated by emission lines and assuming a dust screen following the same reddening law we assume for Galactic extinction. SSP base models were taken from Bruzual & Charlot (2003)[5] for the MILES spectral library (Sánchez-Blázquez et al. 2006) using a Chabrier (2003) stellar initial mass function (IMF) over the range 0.1–100 $M_\odot$. The components for the base models comprised 16 ages from 1 Myr to 13 Gyr for each of four metallicities ($Z = 0.004, 0.008, 0.02, 0.05$). We note that tests with somewhat different base model sets and choice of IMF did not significantly affect continuum subtraction and so do not affect the emission-line results on which our analyses rely. Our procedure

[5] Using the 2016 update at http://www.bruzual.org/bc03/.

largely mirrors that performed on MUSE data of supernova hosts elsewhere (e.g. Galbany et al. 2016a).

3.3 Emission-line fitting

Emission-line fitting was performed on the spectra after subtracting the best-fitting continuum, as determined in Section 3.2. Prior to fitting, the continuum-subtracted spectra were median filtered with a width of 120 Å – this width was chosen in order to remove any broad residuals left by the imperfect continuum fitting, whilst leaving the narrow emission lines unaffected. The emission-line model was a composite model of single Gaussians initially centred at the wavelengths of H β, [O III] $\lambda\lambda$4959,5007, Hα, [N II] $\lambda\lambda$6548,6583 and [S II] $\lambda\lambda$6716,6731 (the two exceptions to this set-up, SNe 2002bp and 2008ge, are detailed later). The fitting was performed via the weighted Levenberg–Marquardt least-squares algorithm. Such fitting is, however, susceptible to finding local minima solutions that are dependent on the initial guesses for the Gaussian parameters. In order to circumvent the dependency on initial guesses, and to restrict to physically plausible solutions we added the following caveats and steps to our fitting routine:

(i) The velocity offset of the Gaussian means were restricted to within 500 km s^{-1} relative to the galaxy's rest frame (i.e. after accounting for the redshift of the galaxy nucleus). This comfortably encloses the limits of rotational velocities seen in late-type galaxies (Sofue & Rubin 2001) whilst preventing misidentification of lines.

(ii) The velocity offset of the Balmer and forbidden lines were each tied, i.e. a single velocity offset for Hα and H β was fit and a separate offset was fit for the other lines.

(iii) The standard deviations of the Gaussians were restricted to $\leq$130 km s^{-1} and pairs of lines for [O III], [N II] and [S II] had tied values for the standard deviation (in km s^{-1}).

(iv) In order to semibrute force locate the global minimum, a list of several initial guesses for each of the means, standard deviations and amplitudes to be fit was made. A grid was then formed of all possible combinations of these parameters to use as initial guesses for the Levenberg–Marquardt fitter, which found the local minimum for each initial guess. The residual between the data and model was used as an estimator of the goodness of fit for each grid position and used to identify the best overall fit.

Where the fitting process failed, we manually inspected the emission-line spectrum. In most cases, low signal to noise or non-detection of the emission features was the cause and we did not consider these bins in our further analysis. Another source of failure was the nuclear bins of some hosts that harbour an active galactic nucleus (AGN). AGN can have a variety of spectral morphologies including broad emission-line components. Their presence prevents much of our emission-line analyses of the host nuclei bins since metallicity and age indicators are calibrated based on ionizing radiation from recently formed young stars, these cases were identified as described in Section 3.3.1.

Observations of UGC 6332, the host of SN 2002bp, were taken under relatively poor sky conditions, and its redshift means that the [S II] λ6731 lies in a region of telluric absorption. We attempted to correct this with MOLECFIT (Smette et al. 2015) using the galaxy nucleus (as there are no bright stars in the MUSE field of view for this host). However, we were not able to clean the spectrum sufficiently to recover the line satisfactorily. Instead, we opted to set the flux of [S II] λ6731 equal to 0.7 $\times$ [S II] λ6716 for each bin. This was chosen as the relation provided a good fit to the vast majority of all other bins in our MUSE sample. We assigned a factor of 2 uncertainty in the estimated flux, which encompasses the range of intensity ratios for this doublet for typical H II regions (Osterbrock & Ferland 2006).

As mentioned, the host of SN 2008ge is an S0 galaxy with the consequential expectation of weak or no emission lines from SF. We found after an initial run with the full emission-line list detailed above that the fitting routine was failing as it relies on finding a fit simultaneously for each line. Thus, although inspection of certain bin spectra showed conspicuous emission in stronger lines (e.g. Hα, [N II]), the fits were failing due to non-detections of the weaker lines. We opted to fit this observation for H β, Hα and N II $\lambda\lambda$6548,6583 only, which allows us to still estimate $E(B-V)^{\rm gas}$ and determine N2 metallicities for the small number of bins where these were detected. This host galaxy is discussed further in Section 6.3.

The fitted Gaussian parameters were used to determine the SNR, flux, equivalent width (EW), FWHM and velocity offset of the lines. Uncertainties on these quantities were found by propagating the statistical uncertainties of the fitted parameters and accounting for photon noise in the manner of Gomes et al. (2016b, and references therein). The Hα and H β fluxes were used to determine the Balmer decrement compared to the expected ratio of 2.86 (assuming Case B recombination, $T_{\rm e} = 10^4$ K and $n_{\rm e} = 10^2$ cm^{-3}; Osterbrock & Ferland 2006) and give the reddening of the gas component, $E(B-V)^{\rm gas}$, again adopting an $R_V = 3.1$ Cardelli et al. (1989) reddening law. This was used to correct the flux and EW values for the effects of dust extinction. Although assumptions for the physical parameters of the gas are inherent to this correction, they are representative of observed H II regions. Furthermore, our metallicity measurements, for example, rely on emission lines nearby in wavelength and as such are largely insensitive to reddening.

Luminosity measurements have their statistical uncertainties quoted; however, the systematic uncertainty due to the distance of the hosts is a dominating source in most cases. For example, a 500 km s^{-1} peculiar galaxy velocity at the median redshift of our sample ($z = 0.0165$) equates to an uncertainty of $\sim$0.084 dex in L(Hα).

3.3.1 *Ionizing source*

We created a BPT diagram (Baldwin, Phillips & Terlevich 1981) for each host, in order to discard bins where the emission lines are not driven by the radiation from young, hot stars, such as regions around AGN, and thus where measures of line strengths and ratios are not appropriate tracers of metallicity, SFR etc. We used the redshift-dependent classification criterion for regular H II regions being powered by SF of Kewley et al. (2013). The theoretically determined limit on the ionization ratios from pure SF is also used (Kewley et al. 2001). We analyse any region below the theoretical SF limit as the region is still consistent with being driven by SF, although there may be smaller contributions from other sources of ionization. Above this limit we consider the ionizing source of the bin to no longer be dominated by SF and do not include these in our results.

An example for the host of SN 2009J, which harbours an AGN and strongly star-forming regions, is shown in Fig. 2. Those bins that were found to be above the theoretical SF line (shown in this plot) were discarded from further analysis as they are powered primarily via other sources of ionization.

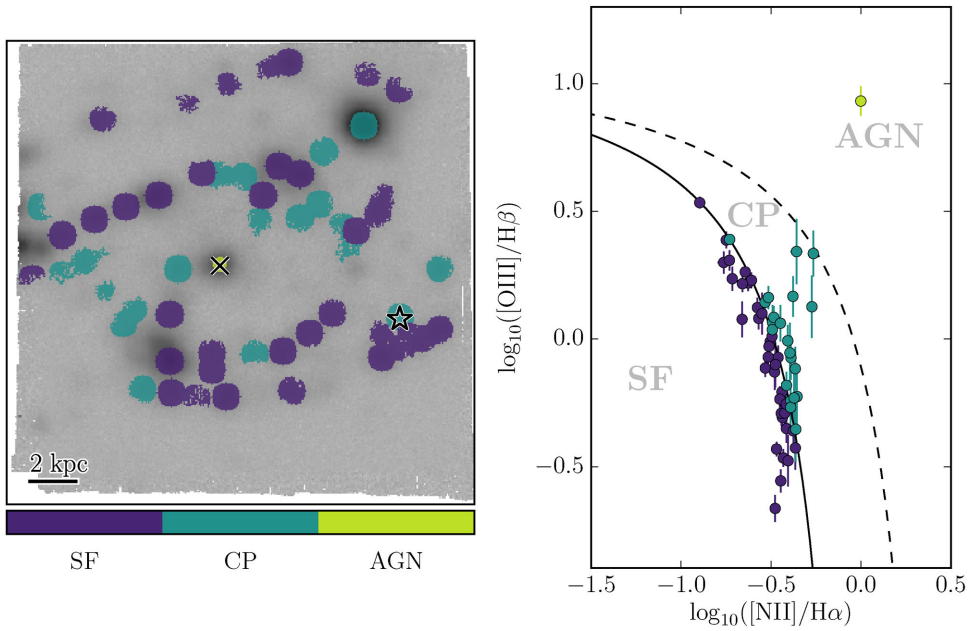

Figure 2. An example BPT map and diagram shown for IC 2160 (the host of SN 2009J). *Left:* heatmap classification of the ionizing source (SF: star formation, CP: composite, AGN: active galactic nucleus) of each bin determined using the relations of Kewley et al. (2001, 2013, see the text), overlaid on an Hα map of the galaxy; north is up, east is left. The location of the host nucleus and the SN explosion site are indicated by the black $\times$ and 'star' symbols, respectively. *Right:* the classification limits for each ionizing source shown for [N II]/Hα and [O III]/H β line ratios with the location of each bin in this parameter space.

3.3.2 *Metallicity*

Many emission-line metallicity abundance indicators are present in the literature, with significant systematic differences in results between methods, in particular based on whether the method is empirical or theoretically motivated (e.g. Kewley & Ellison 2008). The wavelength range of MUSE for low-redshift galaxies covers many emission lines used in various strong emission-line methods for determining the gas-phase metallicity, although it does not extend sufficiently into the blue to cover the most commonly used temperature-sensitive lines – a thorough discussion of metallicity determinations with a view to MUSE data of low-redshift galaxies is given in Krühler et al. (2017). We concentrate here on determining metallicities on the scale of relative oxygen abundance and use the theoretically motivated calibration based on photoionization models presented by Dopita et al. (2016, hereafter D16). This indicator uses the [S II] $\lambda\lambda$6717, 6731 lines as well as Hα and [N II] λ6583 and is thus well suited to MUSE observations of H II regions in the local Universe. The relation is given as

$$12 + \log_{10}(\mathrm{O/H}) = 8.77 + y, \quad (1)$$

where

$$y = \log_{10}\frac{[\mathrm{N\,II}]\lambda6583}{[\mathrm{S\,II}]\lambda\lambda6717,6731} + 0.264 \times \log_{10}\frac{[\mathrm{N\,II}]\lambda6583}{\mathrm{H}\alpha}. \quad (2)$$

This is a good description of the theoretical results over a wide range of metallicities from very subsolar to supersolar. Although this indicator is robust to changing ionization parameter (D16), it was noted by Krühler et al. (2017) that there exists an apparent $\sim$0.15 dex systematic offset to lower abundances with this indicator compared to T_e-based values.

We also present values based on the O3N2 ($= \log_{10}[\frac{[\mathrm{O\,III}]\lambda5007}{\mathrm{H}\beta} \times \frac{\mathrm{H}\alpha}{[\mathrm{N\,II}]\lambda6583}]$) calibration of Marino et al. (2013, hereafter M13),[6] primarily to facilitate the comparison with literature values for the environments of other transient types. There is a 1σ uncertainty of 0.18 dex associated with measurements with this indicator due to the observed spread of T_e-based abundances about this relation. The indicator is given over the Z range $\sim$8.15–8.75 dex. Where literature values were presented in the O3N2 calibration of Pettini & Pagel (2004), we convert these to M13. We adopt a binning regime that means our effective spatial scale is similar to the size of H II regions, and we are therefore not as sensitive to significant variations of the ionization parameter that can occur within individual regions on small spatial scales. For ionization parameter-dependent abundance indicators, such as O3N2, this creates strong gradients within individual regions (Krühler et al. 2017).

Although we correct our emission-line fluxes for reddening [$E(B-V)^{\mathrm{gas}}$ estimated by the Balmer decrement], we note that since the line ratios used in the above metallicity indicators are relatively nearby in wavelength, we are not strongly affected by uncertain reddening values. Individual line flux uncertainties were propagated to calculate the statistical uncertainty on our metallicity measurements.

We determined metallicity gradients for each host with a linear fit to the bin metallicities and deprojected galactocentric distances. Deprojected distances were found following the method of Andersen & Bershady (2013) to determine the position angle and inclination from the velocity map of the Hα line and then normalized by the R_{25} (25th B-band mag arcsec^{-2} surface brightness radius) value of

[6] Where we did not reliably detect [O III] λ5007 in our cubes, we use the N2 relation of M13. These cases are highlighted in tables of results.

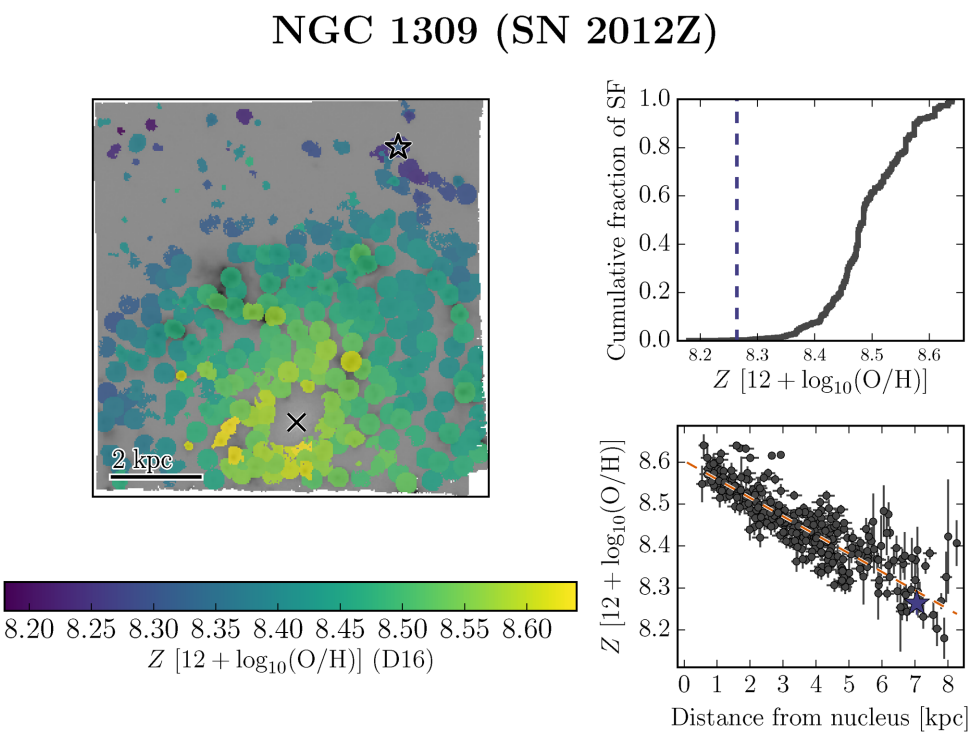

Figure 3. A gas-phase metallicity map for NGC 1309 (the host of SN 2012Z). Metallicities are given on the oxygen abundance scale using the relations of D16. *Left:* a heatmap of the metallicity of each bin overlaid on an H α map of the galaxy; north is up, east is left. The adopted locations of the nucleus and the SN explosion site are indicated by the black $\times$ and 'star' symbols, respectively. *Right:* a cumulative distribution of the metallicity in the galaxy weighted by the SFR – i.e. $L(\mathrm{H}\,\alpha)$ – of each bin *(top)* and the deprojected metallicity gradient of the galaxy *(bottom)*. The SN explosion-site metallicity is highlighted in these panels also.

the host. R_{25} values were taken from NED. For SN 2008ge, the velocity map used was that of the stellar continuum as determined by STARLIGHT. For SNe, where we do not directly detect emission lines at the location of the SN we use these metallicity gradients to estimate the metallicity of the region local to the SN. The uncertainty on this estimate is taken as the rms of the observed metallicity values about the linear fit.

An example of a metallicity map and gradient is shown in Fig. 3 and stamps for all hosts (except SN 2008ge) are given in Appendix C.

3.3.3 SF rates

We use Kennicutt (1998) to convert our extinction-corrected $L(\mathrm{H}\,\alpha)$ values (determined as in Section 3.3) into SFRs with the relation:

$$\mathrm{SFR}\ [\mathrm{M}_\odot\ \mathrm{yr}^{-1}] = 7.9 \times 10^{-42} L(\mathrm{H}\,\alpha)[\mathrm{erg\ s}^{-1}]. \quad (3)$$

3.3.4 Ages

Ages for the youngest SP in galactic regions and at SN explosion sites are often made based on the EW of (primarily Balmer) emission lines in comparison to theoretical predictions. Such mappings between EW values and ages are subject to significant uncertainty due to potentially unaccounted-for effects (stellar multiplicity, SN feedback) and the large spread in physical characteristics of nebular gas in star-forming regions (electron density, physical size). With these caveats in mind, it is nevertheless widely accepted that the EW of nebular emission lines should have some inverse relation with the age of the youngest SP for an instantaneous or rapidly declining SF history for the region. We used results from the Binary Population and Spectral Synthesis code, BPASS (e.g. Eldridge & Stanway 2009, 2012), and processed the stellar continua with CLOUDY (Ferland et al. 1998). This was done with BPASS version 2.1 (Stanway, Eldridge & Becker 2016; Eldridge & Stanway, in preparation) in the manner described in Stanway et al. (2014) for a fiducial nebula gas model of $10^2\ \mathrm{cm}^{-3}$ hydrogen gas density in a spherical distribution with inner radius of 10 pc. From this, we obtained the evolution of EW measurements for H α with age for instantaneous SF episodes, which is shown in Fig. 4. These were compared with our measured EW values at the explosion sites to provide estimates of the age of the youngest SP at these locations. We note here the strong effect of including binary stellar evolution for these calculations, which act to strengthen the emission relative to the continuum, beginning after several Myr. A binary fraction <1.0 would result in evolution somewhere between the two cases shown in Fig. 4. A pertinent study of the effect of including binary stellar evolution when determining age estimates of CCSN-hosting regions has found that regions are generally older than previously thought, and thus revising progenitor initial mass estimates down (Xiao et al. 2017; Xiao et al. in preparation)

3.3.5 Pixel statistics

The location of transients within the light distribution of their hosts has been used to infer further constraints on the nature of the progenitor systems (see Anderson et al. 2015, for a review). We use the normalized cumulative rank (NCR) method presented in James & Anderson (2006): briefly, pixel values for an image of a

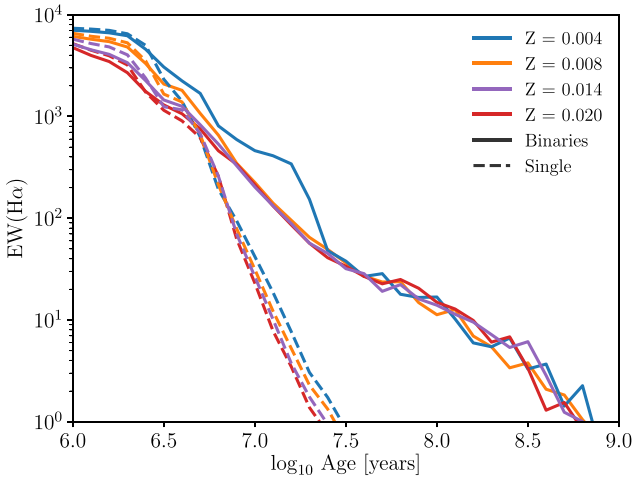

Figure 4. The evolution of EW(H α) for an instantaneous SF episode calculated with BPASS and CLOUDY (see the text). The IMF used has a power-law slope of $\alpha = 2.35$ over the range 0.5–100 $M_{\odot}$. We stress here that this is for a single fiducial gas model of assumed size and density and that the physical properties of the gas distribution can affect results significantly (see Stanway et al. 2014; Eldridge & Stanway, in preparation). Different metallicities are represented by colours with binaries and single populations as solid and dashed lines, respectively.

transient host are sorted, cumulatively summed and then normalized by the total sum of the values. The location of the transient's explosion site in this cumulative sum provides the fraction of light in the host at a level lower than the intensity at the explosion site. When using an appropriate SF tracer, such as H α, the fraction of SF in the host below the level of the explosion site can be inferred; a distribution of H α NCR values describes the association with SF for a sample of transients.

The NCR analysis has been presented for an initial sample of SNe Iax in Lyman et al. (2013). We used the same H α maps constructed from our MUSE data cubes that were used to create our spaxel bins (Section 3.1.1) in order to calculate NCR values for a larger sample of SN Iax. The maps were binned 3 × 3 to circumvent astrometric uncertainties before applying the NCR method. Where we had an existing NCR value from Lyman et al. (2013) and our MUSE observation did not cover the extent of the host, we use the pre-existing value.

We further introduce a metallicity cumulative rank in Section 5.1.3, which we use to assess the presence of metallicity bias in the production of SNe Iax within their host galaxies.

4 NOT DATA ANALYSIS AND METHODS

We here detail the analysis of our NOT observations, highlighting differences from the MUSE analysis. Further details of the analysis methods used can be found in Taddia et al. (2013, 2015a). Prior to analysis, NOT spectra were corrected for Galactic extinction and dereddened in the same manner as the MUSE data cubes. The main differences from the MUSE analysis were the identification of H II regions versus spaxel binning routines and the fitting of emission lines due to a lower spectral resolution. Stellar continuum fitting, identification of the ionizing source and our metallicity, SFR and age measurements followed those described in Section 3.

Intrinsic (deprojected) galactocentric offsets of SN explosion sites and other H II regions were calculated and normalized to R_{25} following the method of Hakobyan et al. (2009, 2012). Host galaxy position angles and inclinations were obtained from NED, supplemented by data from HYPERLEDA,[7] since we were not able to determine a velocity map as was done for the MUSE data (Section 3.3.2). Again, these were normalized by the R_{25} of the hosts. These deprojected distances were used to determine metallicity gradients for the host galaxies where more than two H II regions were extracted. For SNe where we could not extract an H II region underlying the explosion site, we used these gradients to estimate the metallicity of the SN. Statistical uncertainties on these interpolated or extrapolated estimates were determined based on the uncertainties of our linear gradient fit (which generally dominate over the rms of H II regions about the relation, whereas the opposite is true for MUSE, Section 3.3.2).

Since we only have long-slit spectra for these targets, we do not perform our pixel statistics, as done for the MUSE sample (Section 3.3.5).

For two observations, those of UGC 12182 (SN 2014ck) and SDSS J020305.81−035024.5 (SN 2016ado), we were not able to perform our main emission-line-based analysis at any location within the slit due to poor observing conditions. We remove these two events from our sample when discussing our spectroscopic results as they provide no meaningful measurements or limits (however, we include the host-normalized offset of SN 2014ck, $r/R_{25} = 0.18$).

For the hosts of SN 1999ax and PS 15aic, we were only able to extract emission at the host nuclei.[8] As we have no additional spatial information to be gained from the NOT long-slit spectra, we opted to use existing SDSS spectra that offer improved spectral resolution and depth on which to perform our analysis.

For SN 2009ku and PS 15csd, we take the host nucleus measurements as those of the SN explosion site owing to the small apparent size of the hosts and the very small offset of the SNe.

Within our NOT-observed sample, we have two duplicates of MUSE-observed events: SNe 2002cx and 2015H. We found very good agreement (within 1σ) between our results obtained for the explosion site of SN 2002cx and host nuclei of each (the explosion site of SN 2015H was not detected in emission lines in the NOT data) for the two sets of data. We present our results for these SNe based on the MUSE data results since these are subject to smaller statistical uncertainties owing to greater signal to noise of the emission lines and increased spectral resolution, and also allowed for more robust determinations of the metallicity gradients as more H II regions could be analysed.

4.1 H II region identification

We performed an inspection of each acquisition image as well the H α line flux trace in order to identify H II regions from which to extract spectra (i.e. peaks in the flux trace). An example of this procedure is shown in the top of Fig. 5, extraction widths were ad hoc in order to maximize the SNR.

For our observation of SN 2008A, the slit did not cover the host nucleus and thus we do not have a measurement of the nucleus for this host.

[7] http://atlas.obs-hp.fr/hyperleda/

[8] For SN 1999ax, we additionally detect another nearby source of H II at an apparently higher redshift, this is discussed in Section 6.4.

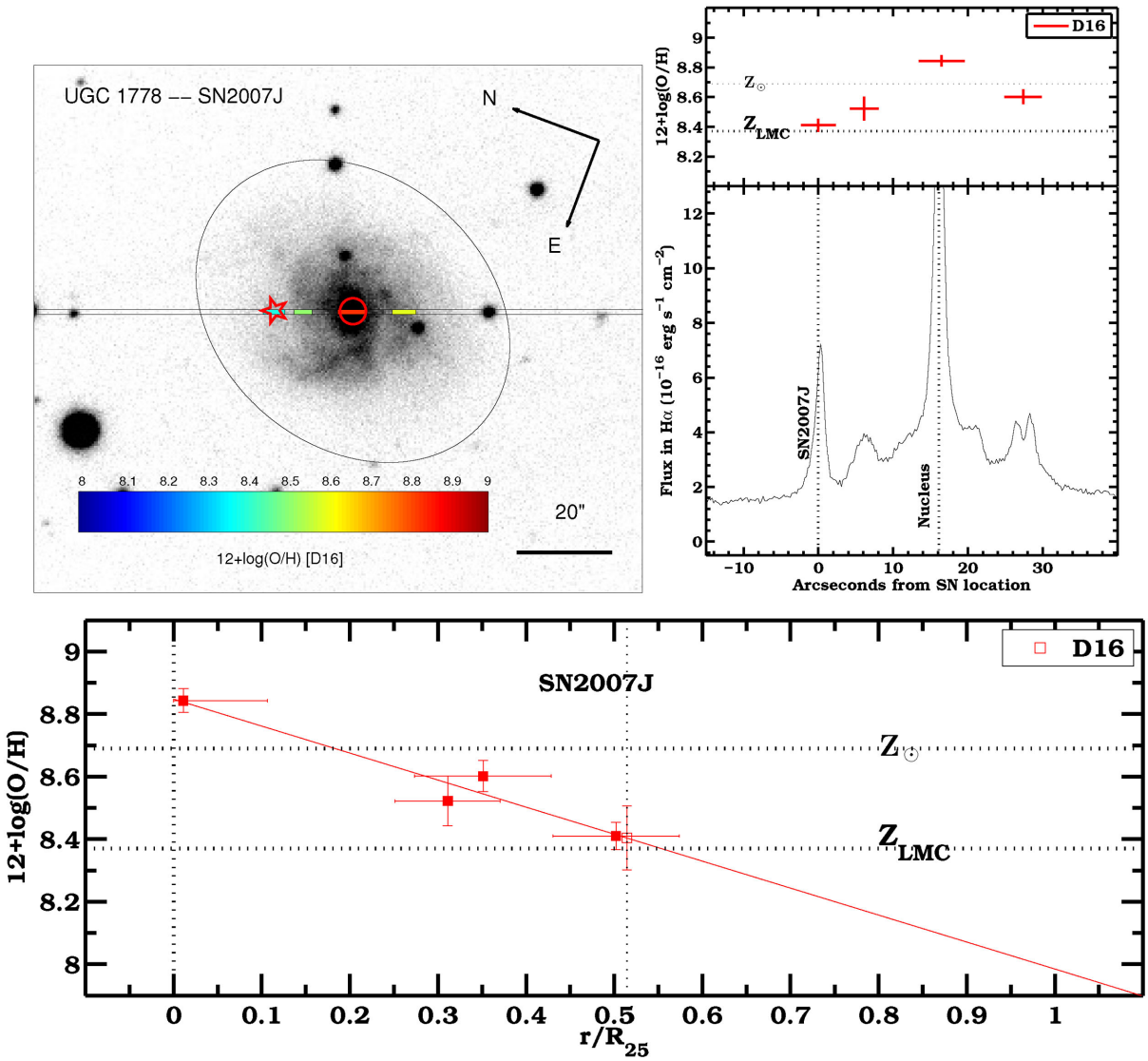

Figure 5. An example of the analysis performed on our NOT observations for UGC 1778 (the host of SN 2007J). *Top left:* the open filter acquisition image. Overlaid are the 25th *B*-band magnitude elliptic contour (black solid line), the position of SN 2007J (red star) and the centre of the galaxy (red circle). The slit position is shown, and a colour code is used to show the D16 metallicity measurements at the position of each H II region that we inspected. *Top right:* the flux at H α along the slit, with the location of the SN and host nucleus marked. The D16 metallicity measurements are shown at the corresponding positions in the top subpanel. *Bottom:* the metallicity gradient of UGC 1778. The linear fit on our D16 measurements is shown with a solid red line. The interpolated metallicity at the SN distance is marked with an empty red square and its uncertainty corresponds to the fit error. The positions of SN and nucleus are marked with vertical dotted lines. The solar metallicity and the LMC metallicity are indicated with horizontal dotted lines.

4.2 Emission line fitting

Emission line fitting followed broadly the same methodology as for the MUSE spectra (Section 3.3); however, the lower resolution of the NOT spectra meant we had to use a different fitting routine as nearby lines are blended. First, the H α and [N II] $\lambda\lambda$6548,6583 lines were simultaneously fit with the Gaussians of fixed width (determined by the spectral resolution) and fixed centroid offsets using the known wavelengths of the lines. Furthermore, the flux of [N II] λ6548 was fixed as one-third that of [N II] λ6583 (Osterbrock & Ferland 2006) – this assumption was required to allow for a proper fit of this faint line, although it is not used in our metallicity determinations, to remove its contamination from H α. Similarly, the [S II] $\lambda\lambda$6716,6731 doublet was fitted with two Gaussians of fixed width and separation. We also attempted fits to H β, [O III] λ5007 for each extracted spectrum, however, due to poorer sensitivity in the blue part of the spectrum we were not able to measure these in several cases.

The poorer spectral resolution of the NOT spectra may introduce some additional sources of uncertainty but we are confident in our fitted values none the less. For example, the assumption of a [N II] λ6583/λ6548 line ratio and the adoption of fixed widths for the Gaussian describing each transition line are valid approximations for a variety of star-forming regions, as found from our MUSE results (e.g. Table B1). Indeed, as detailed in Section 4, we had two events with observations by both MUSE and NOT. Our results from NOT spectra agreed within 1σ of our MUSE measurements for SN 2002cx and SN 2015H, indicating the lower spectral resolution is not compromising our results.

Table 4. Results for SN explosion sites and host nuclei.

Galaxy	SN	Offset[a] (R_{25})	L(H α) ($\log_{10}$ erg s^{-1})	EW(H α) (Å)	NCR	Z (SN site)[b] D16	Z (SN site)[b] M13	Z (Host nucleus)[c] D16	Z (Host nucleus)[c] M13
				MUSE sample					
IC 344	1991bj	1.383	39.40 ± 0.01	98.9 ± 3.4	0.29	8.26 ± 0.01	8.37 ± 0.01	8.55 ± 0.01	8.51 ± 0.01
UGC 6332	2002bp	0.920	37.13 ± 0.36	1.8 ± 1.5	0.00	–	8.77 ± 0.25[d]	AGN	
CGCG 044-035	2002cx	0.765	39.19 ± 0.01	45.8 ± 1.9	0.33	8.25 ± 0.02	8.36 ± 0.01	8.52 ± 0.01	8.50 ± 0.01
UGC 11001	2004cs[e]	0.519	39.23 ± 0.01	78.6 ± 2.2	0.72	8.42 ± 0.02	8.43 ± 0.01	8.68 ± 0.01	8.56 ± 0.02
NGC 5468	2005P	0.443	37.50 ± 0.02	9.2 ± 0.9	0.06[f]	8.07 ± 0.13	8.36 ± 0.06	Not in FOV	
UGC 272	2005hk	1.089	37.25 ± 0.04	20.9 ± 5.1	0.00	7.85 ± 0.28	8.34 ± 0.09	8.39 ± 0.02	8.45 ± 0.01
IC 577	2008ae	0.881	39.06 ± 0.01	58.6 ± 5.4	0.07	8.66 ± 0.03	8.50 ± 0.02	8.99 ± 0.04	8.53 ± 0.01
NGC 1527	2008ge	0.055	–	–	0.00	–	–	–	–
UGC 12682	2008ha	0.263	37.91 ± 0.01	24.9 ± 1.0	0.41[f]	7.91 ± 0.04	8.22 ± 0.01	7.99 ± 0.02	8.19 ± 0.00
IC 2160	2009J	0.551	38.81 ± 0.01	34.3 ± 1.7	0.00[f]	8.51 ± 0.03	8.41 ± 0.02	AGN	
ESO 162-017	2010ae	0.070	39.24 ± 0.01	39.7 ± 0.8	0.61	8.26 ± 0.01	8.32 ± 0.00	8.28 ± 0.01	8.31 ± 0.00
NGC 1566	2010el	0.106	38.66 ± 0.01	20.4 ± 0.6	0.03	8.85 ± 0.02	8.51 ± 0.02	AGN	
NGC 6708	2011ce	0.136	39.94 ± 0.01	86.4 ± 1.9	0.59	8.76 ± 0.01	8.59 ± 0.01	8.88 ± 0.01	8.60 ± 0.02
NGC 1309	2012Z	0.766	37.80 ± 0.01	36.1 ± 1.9	0.00[f]	8.26 ± 0.03	8.41 ± 0.01	AGN	
ESO 114-007	2013gr	0.266	37.78 ± 0.01	31.0 ± 1.5	0.06	7.84 ± 0.05	8.27 ± 0.01	7.96 ± 0.03	8.27 ± 0.01
NGC 4303	2014dt	0.218	38.78 ± 0.01	33.0 ± 0.6	0.04	8.85 ± 0.02	8.52 ± 0.02	not in FOV	
CGCG 048-099	2014ey	0.616	38.87 ± 0.01	47.8 ± 3.6	0.22	8.36 ± 0.04	8.43 ± 0.02	8.67 ± 0.01	8.57 ± 0.02
NGC 3464	2015H	0.426	37.97 ± 0.02	7.6 ± 0.4	0.01	8.66 ± 0.07	8.50 ± 0.10	8.97 ± 0.05	8.58 ± 0.01[d]
				NOT sample					
SDSS J140358.27+155101.2	1999ax	–	–	–	–	–	–	7.78 ± 0.10	8.23 ± 0.02
NGC 7407	2003gq	0.133	39.57 ± 0.01	23.5 ± 0.9	–	8.51 ± 0.07	8.33 ± 0.02[d]	AGN	
CGCG 283-003	2004gw	0.568	–	–	–	–	–	9.23 ± 0.24	8.54 ± 0.02
NGC 5383	2005cc	0.061	38.81 ± 0.01	28.7 ± 0.4	–	8.80 ± 0.07	8.50 ± 0.02[d]	8.86 ± 0.08	8.51 ± 0.02[d]
UGC 6154	2006hn	0.498	38.98 ± 0.01	18.4 ± 0.6	–	8.81 ± 0.17	8.50 ± 0.02	8.95 ± 0.05	8.48 ± 0.01
UGC 1778	2007J[e]	0.514	39.35 ± 0.01	116.9 ± 9.4	–	8.41 ± 0.04	8.38 ± 0.02	8.84 ± 0.04	8.45 ± 0.01
SDSS J020932.73−005959.8	2007qd	0.531	–	–	–	–	–	8.54 ± 0.03	8.46 ± 0.01
NGC 634	2008A	0.789	–	–	–	–	–	not in FOV	
APMUKS(BJ) B032747.73-281526.1	2009ku[g]	–	40.41 ± 0.01	47.86 ± 0.82	–	8.43 ± 0.06	8.37 ± 0.01	8.43 ± 0.06	8.37 ± 0.01
NGC 2315	2011ay	0.468	–	–	–	–	–	–	8.69 ± 0.01
CGCG 205-021	PS1-12bwh	0.318	–	–	–	–	–	8.98 ± 0.07	8.56 ± 0.01
NGC 5936	2013dh	0.219	39.14 ± 0.01	34.3 ± 3.7	–	8.77 ± 0.05	8.58 ± 0.01	9.18 ± 0.03	8.63 ± 0.01
UGC 11369	2013en	0.480	39.32 ± 0.01	20.7 ± 0.7	–	8.48 ± 0.09	8.46 ± 0.03[d]	9.05 ± 0.02	8.63 ± 0.01[d]
UGC 12850	2014ek	0.248	39.83 ± 0.01	34.8 ± 0.4	–	–	8.50 ± 0.02[d]	AGN	
UGC 12156	2015ce	0.394	–	–	–	–	–	8.92 ± 0.09	8.63 ± 0.01
SDSS J133047.95+380645.0	PS 15aic	0.666	39.50 ± 0.02	2.3 ± 0.1	–	–	–	–	8.72 ± 0.02[d]
SDSS J020455.52+184815.0	PS 15csd[g]	–	39.55 ± 0.02	25.1 ± 1.0	–	8.11 ± 0.17	8.29 ± 0.03	8.11 ± 0.17	8.29 ± 0.03

Notes. [a]The deprojected offset of the explosion site normalized by the R_{25} value of the host.
[b]The 12 + $\log_{10}$(O/H) abundance measured in the scales of D16 and M13 for the SN explosion site. Uncertainties are statistical only: M13 have a systematic uncertainty of 0.18 dex; D16 do not have well-quantified systematics but appear lower than T_e-based estimates (Krühler et al. 2017).
[c]As for [b] but for the host nucleus. 'AGN' means the host was deemed to host an active galactic nucleus, 'not in FOV' means the host nucleus was not captured in the IFU or slit.
[d]The N2 relation of M13 was used instead of O3N2.
[e]Helium detected in SN spectra.
[f]NCR value taken from Lyman et al. (2013).
[g]Due to the SN being overlaid on the nucleus of an unresolved host at very small offset, we use the host nucleus results as those of the SN site also.

5 RESULTS

We present our main results of the SNe explosion sites and host nuclei in Table 4. Individual line fluxes for the explosion sites (where they could be measured) are given in Table B1.

We indicate those observations where the host nucleus was not captured in the FOV or where the ionizing source was deemed to be powered by an AGN (Section 3.3.1 and Fig. 2). We find that 19 per cent of our sample (where our observations covered the host nucleus) have an AGN. Given the presence of several irregular galaxies, likely to be of fairly low masses, in the sample, such an AGN fraction is typical of the local Universe (Kauffmann et al. 2003). For comparison, the AGN fractions of star-forming SN Ia, Ib/c and II hosts are ∼ 59, 32 and 22 per cent, respectively (Galbany et al. 2016b). However, these values were derived from within the sample of CALIFA galaxies (Sánchez et al. 2012a) and so

underrepresent small, faint (low-mass) galaxies, for which the AGN fraction is significantly depressed (Kauffmann et al. 2003). Additionally, the SN Iax discoveries come from a mixture of transient survey strategies, including galaxy-targeted searches, further complicating a comparison of the unbiased host galaxy AGN fractions for the existing samples.

5.1 Metallicity

5.1.1 Gradients and estimating explosion-site metallicities

In some cases, we were not able to directly measure emission lines at the explosion site of the SN. As discussed in Section 4, in these cases we resort to estimating the metallicity based on the observed metallicity gradient of the galaxy as has been done previously for other studies of SN environments.

Here, we utilize the power of the MUSE data, in combination with the results of NOT to assess the reliability of this method in the extreme regimes of many and few H II regions from which to determine the gradient. In Table 5, we present our determined metallicity gradients alongside the estimated (based on the gradient) and measured metallicities of the SN explosion sites, which are plotted in Fig. 6.[9] The estimates agree very well with the measured values – the one outlier in the figure is SN 2005P, although this is still only at the $\sim 2.3\sigma$ level and interestingly only in the D16 indicator. We crucially also see that even with a low number of regions from which to fit a metallicity gradient (in the case of NOT data), the measured and estimated values agree well, offering further support of results derived using this method. The associated uncertainties (determined from the residuals of the measured H II region metallicities about the gradient or based on the uncertainties of the linear fit; Sections 3 and 4) are generally larger than the statistical uncertainties on the measured values, but are still mainly dominated by the systematic uncertainties on the calibrations. We note that these findings corroborate those of Galbany et al. (2016b) who investigated a number of local metallicity estimators in IFS data, finding that an interpolation of the metallicity gradient is a robust estimate.

For some observations, we were not able to either measure the metallicity at the SN explosion site or determine a metallicity gradient. In the cases of SNe 1999ax, 2009ku, PS 15aic and PS 15csd, we were only able to measure the host nucleus metallicities, and for SN 2008A we could only measure a single bright H II region slightly offset from the host nucleus.[10] SN 2009ku and PS 15csd lie on top of their respective hosts that are of small apparent size and so we adopt the host nucleus metallicities as those of the SN (Table 4). Our determined metallicity gradients cover a large range, making any estimates for SNe 1999ax, 2008A or PS 15csd based on an average gradient of limited use as the associated error would be very large (Galbany et al. 2016b also caution against this methodology). We are limited to supposing that their metallicities are less than or equal to their respective host nucleus metallicities (for SN 2008A our sole H II region metallicity is at an offset of $r/R_{25} = 0.168$ with a metallicity of $Z_{\rm D16} = 9.10 \pm 0.07_{\rm stat}$ dex, $Z_{\rm M13,\,N2} = 8.60 \pm 0.01_{\rm stat}$ dex). This does not introduce the requirement for especially low metallicities (compared to the rest of the sample) for these events.

Given the very good agreement between our direct explosion-site metallicities and those estimated based on the hosts' gradients, we supplement our explosion-site metallicity values with gradient estimates where appropriate, and present and discuss this enlarged sample in our results.

5.1.2 Distribution

In Fig. 7, the metallicity distribution of SNe Iax explosion sites is shown alongside that of the host nuclei and all H II regions extracted in our MUSE sample.[11] The cumulative weight of each H II region in this plot is given by its H α luminosity, i.e. SFR, in order to show the cumulative distribution of SFR with metallicity in SN Iax hosts. Although we only have global metallicity determinations for the MUSE half of our sample, the main discriminating factor between this and the NOT sample is only declination of the source, and so we expect no bias in terms of host properties. Additionally, a few of our MUSE observations do not cover the entire hosts, but they do cover areas around the same location and offset as the SNe, and cover reasonable fractions of their respective hosts. As a check, we also plot in Fig. 7 the metallicity distribution of SF in our MUSE sample only including observations that cover approximately all the host galaxy (i.e. we exclude observations of SNe 2005P, 2010el, 2012Z, 2013gr and 2014dt; see Fig. C1). The distribution for this subsample of our MUSE galaxies is almost identical to the full MUSE sample (as was found in our other environmental measure also) and so the partially covered hosts do not introduce significant biases into the distributions.

We find that the metallicity of SNe Iax sites are at lower metallicities than where typical SF is occurring in the hosts (in each metallicity indicator shown the KS test gives $p \sim 0.01$ that the two are drawn from the same distribution). As expected, given the SN explosion sites are offset from their host nuclei and we find mostly negative radial metallicity gradients in our hosts, there is an offset between the host nuclei and explosion-site metallicities.

5.1.3 Metallicity ranking of explosion sites

In order to further assess the indications of Section 5.1.2, we have calculated SFR-weighted metallicity NCR (*Z*NCR) values for the explosion sites of out MUSE sample of SNe Iax. The *Z*NCR is calculated in a similar manner to the traditional NCR value of SNe (Section 3.3.5, see also James & Anderson 2006; Anderson et al. 2012), but the cumulative distribution of the SFR-weighted metallicity in the galaxy is used to determine the rank of each SN. The *Z*NCR is thus the fraction of stars being formed at or below the metallicity of the explosion site in that host. This may be seen visually in the top right panel of Fig. 3, where the SN in question has *Z*NCR = 0.003. In Fig. 8, we show the distributions of *Z*NCR for D16 and M13. In the case of metallicity-unbiased formation of the progenitors, a uniform distribution (indicated by dashed lines) should be recovered, i.e. the SNe have no dependence on where in the metallicity distribution of SF they form, and so sample it

[9] We exclude NGC 1527, the host of SN 2008ge, as even if the ionized gas we detect is driven by SF (see Section 6.3), it is very irregular in morphology, and perhaps not intrinsic to the luminous S0 host. Thus, a metallicity gradient is not likely to be an appropriate description.

[10] In agreement with our findings based on the NOT spectroscopy here, Lyman et al. (2013) show an H α image of the SN location with no underlying detected emission and mainly faint, diffuse emission throughout the host. McCully et al. (2014b) also present *HST* broad-band observations of the environment, showing it to be in the outskirts of its host, in a fairly low-density environment.

[11] We do not include the emission from the host of SN 2008ge; see Section 6.3.

Table 5. Metallicity gradients for SN Iax host galaxies and SN explosion-site metallicities. The metallicity gradients for SN Iax host galaxies are parametrized as $Z = m/R_{25} \times D + c$, where D is the deprojected offset normalized by the host R_{25}, in the scales of D16 and M13. $Z_{SN,grad}$ are estimates of Z based on these metallicity gradients at the offset of the SN, and $Z_{SN,meas}$ are our directly measured values for the H II underlying the SN position.

Galaxy	SN name	D16				M13			
		m/R_{25}	c	$Z_{SN,grad}$	$Z_{SN,meas}$	m/R_{25}	c	$Z_{SN,grad}$	$Z_{SN,meas}$
MUSE sample									
IC 344	1991bj	-0.27 ± 0.08	8.59 ± 0.08	8.22 ± 0.05	8.26 ± 0.01	-0.13 ± 0.07	8.51 ± 0.06	8.33 ± 0.04	8.37 ± 0.01
UGC 6332[a]	2002bp	0.07 ± 0.19	8.82 ± 0.12	8.88 ± 0.08	–	0.01 ± 0.06	8.56 ± 0.04	8.57 ± 0.02	8.77 ± 0.25
CGCG 044-035	2002cx	-0.43 ± 0.11	8.54 ± 0.05	8.21 ± 0.03	8.25 ± 0.02	-0.18 ± 0.08	8.49 ± 0.03	8.35 ± 0.02	8.36 ± 0.01
UGC 11001	2004cs	-0.28 ± 0.13	8.62 ± 0.07	8.47 ± 0.05	8.42 ± 0.02	-0.22 ± 0.07	8.56 ± 0.04	8.45 ± 0.02	8.43 ± 0.01
NGC 5468	2005P	-0.68 ± 0.15	8.70 ± 0.08	8.40 ± 0.05	8.07 ± 0.13	-0.38 ± 0.10	8.57 ± 0.05	8.40 ± 0.04	8.36 ± 0.06
UGC 272	2005hk	-0.38 ± 0.10	8.30 ± 0.06	7.88 ± 0.05	7.85 ± 0.28	-0.18 ± 0.08	8.41 ± 0.05	8.22 ± 0.04	8.34 ± 0.09
IC 577	2008ae	-0.23 ± 0.11	8.88 ± 0.07	8.68 ± 0.04	8.66 ± 0.03	-0.17 ± 0.05	8.64 ± 0.04	8.49 ± 0.03	8.50 ± 0.02
UGC 12682	2008ha	-0.14 ± 0.13	7.97 ± 0.07	7.93 ± 0.07	7.91 ± 0.04	-0.06 ± 0.12	8.25 ± 0.06	8.24 ± 0.05	8.22 ± 0.01
IC 2160	2009J	-0.79 ± 0.23	8.97 ± 0.10	8.53 ± 0.06	8.51 ± 0.03	-0.50 ± 0.20	8.66 ± 0.10	8.38 ± 0.05	8.41 ± 0.02
ESO 162-017	2010ae	-0.24 ± 0.17	8.26 ± 0.07	8.24 ± 0.06	8.26 ± 0.01	-0.08 ± 0.16	8.35 ± 0.06	8.35 ± 0.05	8.32 ± 0.01
NGC 1566	2010el	-0.64 ± 0.75	8.91 ± 0.10	8.84 ± 0.05	8.85 ± 0.02	0.13 ± 0.44	8.55 ± 0.07	8.57 ± 0.03	8.51 ± 0.02
NGC 6708	2011ce	-0.54 ± 0.10	8.85 ± 0.05	8.78 ± 0.04	8.76 ± 0.01	-0.30 ± 0.09	8.62 ± 0.04	8.58 ± 0.04	8.59 ± 0.01
NGC 1309	2012Z	-0.41 ± 0.14	8.60 ± 0.05	8.29 ± 0.05	8.26 ± 0.03	-0.24 ± 0.10	8.55 ± 0.04	8.37 ± 0.03	8.41 ± 0.01
ESO 114-007	2013gr	-0.23 ± 0.14	7.99 ± 0.06	7.93 ± 0.06	7.84 ± 0.05	-0.16 ± 0.18	8.29 ± 0.08	8.24 ± 0.07	8.27 ± 0.01
NGC 4303	2014dt	-0.27 ± 0.30	8.88 ± 0.07	8.82 ± 0.05	8.85 ± 0.02	0.07 ± 0.28	8.55 ± 0.07	8.57 ± 0.03	8.52 ± 0.02
CGCG 048-099	2014ey	-0.36 ± 0.09	8.65 ± 0.06	8.42 ± 0.06	8.36 ± 0.04	-0.17 ± 0.07	8.51 ± 0.06	8.40 ± 0.05	8.43 ± 0.02
NGC 3464	2015H	-0.51 ± 0.20	8.92 ± 0.08	8.70 ± 0.05	8.66 ± 0.07	-0.52 ± 0.11	8.77 ± 0.05	8.55 ± 0.03	8.50 ± 0.10
NOT sample									
NGC 7407[a]	SN 2003gq	-0.04 ± 0.43	8.61 ± 0.13	8.60 ± 0.14	8.51 ± 0.07	0.30 ± 0.32	8.38 ± 0.10	8.42 ± 0.11	8.33 ± 0.02
CGCG 283-003[a]	SN 2004gw	-1.21 ± 0.21	9.18 ± 0.07	8.03 ± 0.21	–	-0.12 ± 0.08	8.51 ± 0.02	8.39 ± 0.08	–
NGC 5383[a]	SN 2005cc	-0.97 ± 0.21	8.86 ± 0.01	8.80 ± 0.02	8.80 ± 0.07	-0.30 ± 0.30	8.51 ± 0.01	8.49 ± 0.02	8.50 ± 0.02
UGC 6154	SN 2006hn	-0.14 ± 0.03	8.94 ± 0.02	8.82 ± 0.03	8.81 ± 0.17	0.06 ± 0.10	8.49 ± 0.06	8.55 ± 0.11	8.50 ± 0.02
UGC 1778	SN 2007J	-0.86 ± 0.16	8.85 ± 0.06	8.40 ± 0.10	8.41 ± 0.04	-0.13 ± 0.02	8.45 ± 0.01	8.38 ± 0.01	8.38 ± 0.02
SDSS J020932.73-005959.8[a]	SN 2007qd	0.07	8.54	8.60 ± 0.15[b]	–	0.04	8.46	8.50 ± 0.15[b]	–
NGC 2315[a]	SN 2011ay	–	–	–	–	-0.42	8.69	8.50 ± 0.15[b]	–
CGCG 205-021[a]	PS1-12bwh	-0.42	8.98	8.84 ± 0.15[b]	–	0.00 ± 0.05	8.51 ± 0.04	8.51 ± 0.04	–
NGC 5936	SN 2013dh	-1.92 ± 0.55	9.17 ± 0.10	8.75 ± 0.16	8.77 ± 0.05	-0.21 ± 0.02	8.63 ± 0.00	8.59 ± 0.00	8.58 ± 0.01
UGC 11369[a]	SN 2013en	-0.96 ± 0.37	9.07 ± 0.14	8.61 ± 0.24	8.48 ± 0.09	-0.28 ± 0.11	8.63 ± 0.04	8.50 ± 0.07	8.46 ± 0.03
UGC 12850[a]	SN 2014ek	–	–	–	–	-0.00 ± 0.03	8.48 ± 0.02	8.48 ± 0.02	8.50 ± 0.02
UGC 12156[a]	SN 2015ce	-1.49 ± 0.25	8.88 ± 0.08	8.29 ± 0.13	–	-0.36 ± 0.16	8.61 ± 0.05	8.46 ± 0.08	–

Notes. [a]The N2 relation of M13 was used instead of O3N2.
[b]Only two H II regions were used to determine the gradient. We adopt an uncertainty of ± 0.15 dex on $Z_{SN,grad}$.

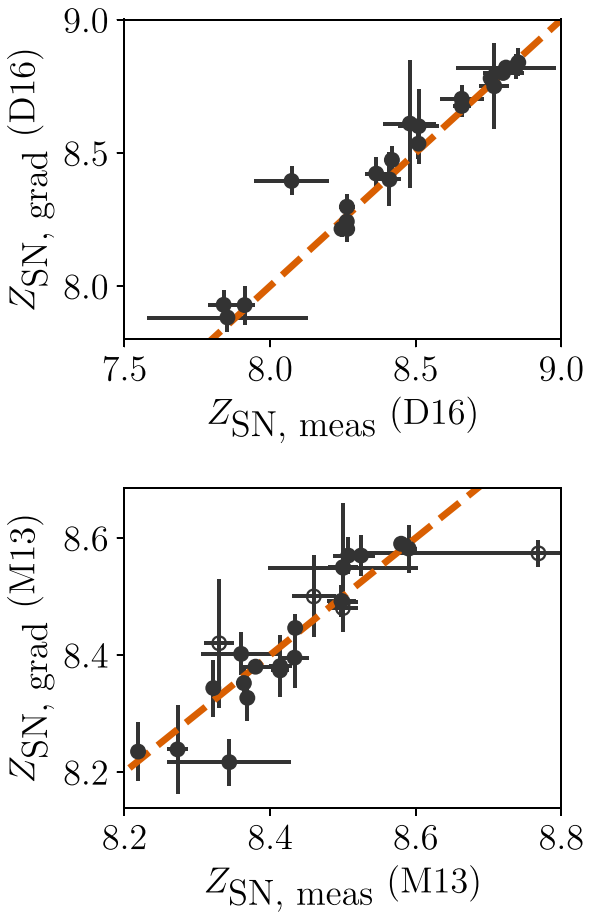

Figure 6. A comparison between the metallicity determined directly at the location of SN explosion sites ($Z_{SN,\,meas}$) and that which would be estimated based on the metallicity gradient alone ($Z_{SN,\,grad}$). Metallicities are determined using the calibrations of D16 and M13 in the top and bottom panels, respectively. Empty markers in the lower panel indicate the N2 relation was used (versus O3N2 for filled markers). Uncertainties on the measured metallicities are statistical only. The gradient uncertainties are either the uncertainty on the gradient linear fit, or the root mean square of H II region metallicity residuals about the gradient (see the text). Orange dashed lines indicate the one to one relation for each.

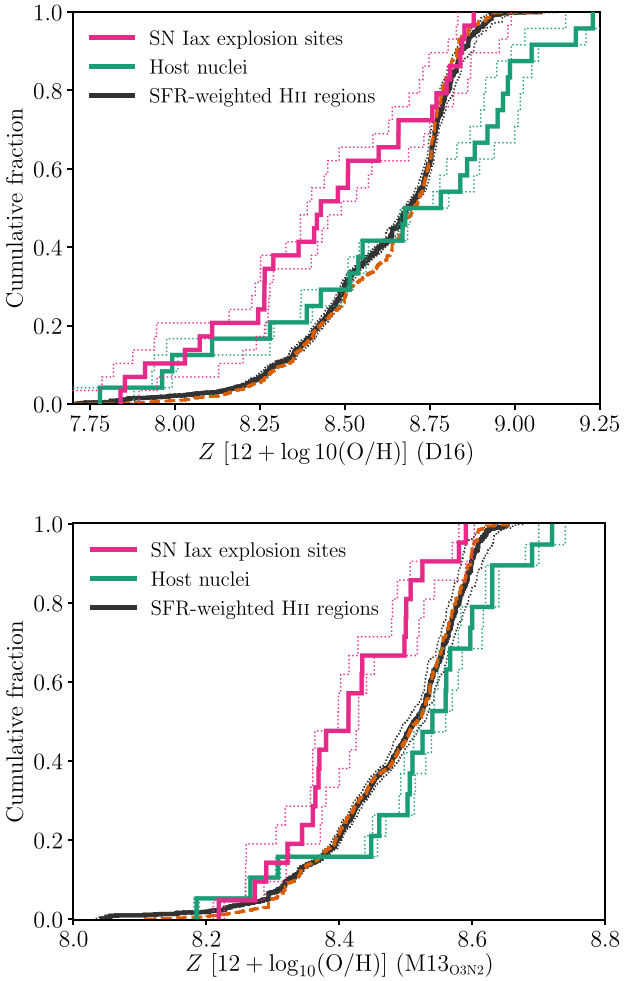

Figure 7. The metallicity distributions of SNe Iax explosion sites, their host nuclei, and all detected H II regions in the MUSE sample. Metallicities are determined using the calibrations of D16 and M13 (O3N2) in the top and bottom panels, respectively. When appropriate, SN explosion-site metallicity estimates based on the gradients of the hosts are included (see Section 5.1.1). Dotted lines are the distributions after adding/subtracting 1σ statistical uncertainties to/from all values and are somewhat extreme limits for the true distribution. The cumulative sum of SN explosion sites and host nuclei are unweighted (i.e. a step in these histograms equals one SN or host nucleus, as appropriate). The H II regions have been weighted by their Hα luminosity such that this histogram shows the cumulative fraction of all detected SF with metallicity across the MUSE sample. The thin orange dashed line shows the subsample of MUSE H II regions for which the observations covered the whole host and appears almost indistinguishable from the full H II region sample (see the text).

uniformly. We see for both distributions the SN explosion sites are systematically shifted to lower values than the uniform distribution, indicating the SNe are preferentially exploding in metal-poor regions, and not unbiasedly tracing the SF in their hosts. For M13, although the distribution is systematically below the uniform distribution, the difference is more marginal than for D16.

5.2 Ages and SFR

We show the EW(Hα) and L(Hα) measurements for our explosion-site bins in Figs 9 and 10, respectively. As was done for the metallicities, we also show the cumulative distribution of SF in these measurements for our MUSE-observed hosts. The regions of SF at the locations of SNe Iax are occurring at significantly lower EW and luminosities than the overall SF in the hosts (KS test $>3\sigma$ for each). Adopting an Hα luminosity–SFR relation (Kennicutt 1998), the Hα luminosities imply that the explosion sites are typically of lower SFR than that of the population of SF regions in the hosts, ranging from 10^{-4} to 10^{-2} M$_\odot$ yr^{-1}.

As discussed in Section 3.3.4, ages for the young stellar component of star-forming regions can be estimated from EW measurements of emission lines but are subject to sources of uncertainty. The bulk of our explosion-site EW(Hα) measurements are ∼tens up to ∼100 Å. We show in Fig. 4 (see Section 3.3.4) the evolution of EW(Hα) with age for BPASS models for an instantaneous SF episode at a range of metallicities. As the consensus is that the vast majority of (particularly massive) stars are in some form of binaries (e.g. Sana et al. 2012) we compare results with the binary population models.

Our observed range of EW(Hα) suggests young SP components of several $\times10^7$–10^8 yr at the locations of SNe Iax. We again note

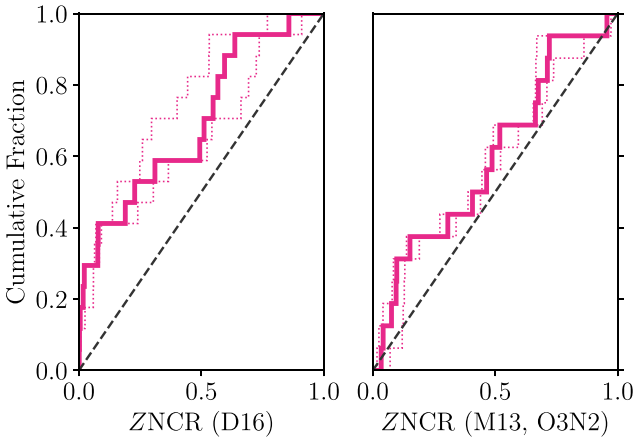

Figure 8. The ZNCR values of SNe Iax explosion sites in two metallicity indicators, as observed with MUSE. In the case of metallicity-unbiased production of the progenitors, the SNe should create a uniform distribution in ZNCR (thick dashed lines). Uncertainties on the distributions were found by creating many realizations of the cumulative sums (based on the uncertainties of the values) for each SN host and recalculating each explosion site's rank. Dotted lines represent the lower and upper distributions of the 95 per cent confidence interval of the ranks.

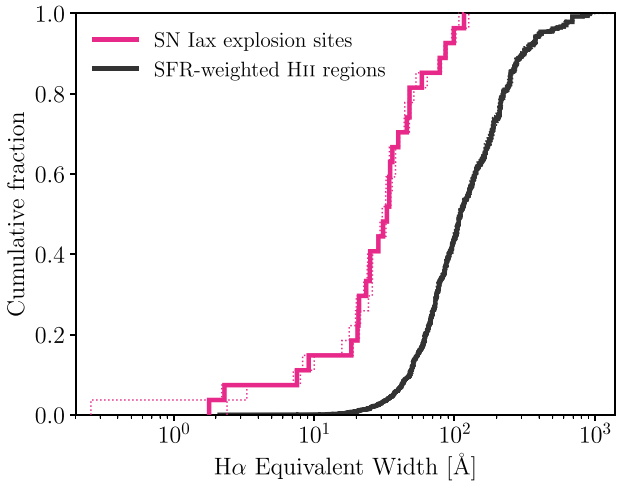

Figure 9. As for Fig. 7 but here showing EW(H α) of SN Iax explosion sites.

the inherent uncertainties in selecting a single fiducial model for the nebular gas properties; however, these values indicate that there are moderately young SP components at the location of the majority of SNe Iax explosion sites.[12] Notably, although our EW values are actually somewhat lower limits of the true young SP EW (as there will be an existing underlying, older SP that contributes to the continuum but not emission lines), they are not exceptionally high. This would seem to disfavour very young, and therefore very massive, SPs at their locations with ages of several Myr, since

[12] Although we were not able to measure emission lines at the locations of some NOT-observed examples, these data were comparatively shallower than the MUSE data, where signatures of ongoing SF were found for all but one explosion site (SN 2008ge). This is demonstrated by our duplicate observations of SN 2015H: in the NOT data, we were not able to extract an emission line spectrum at the explosion site but we could in the MUSE data.

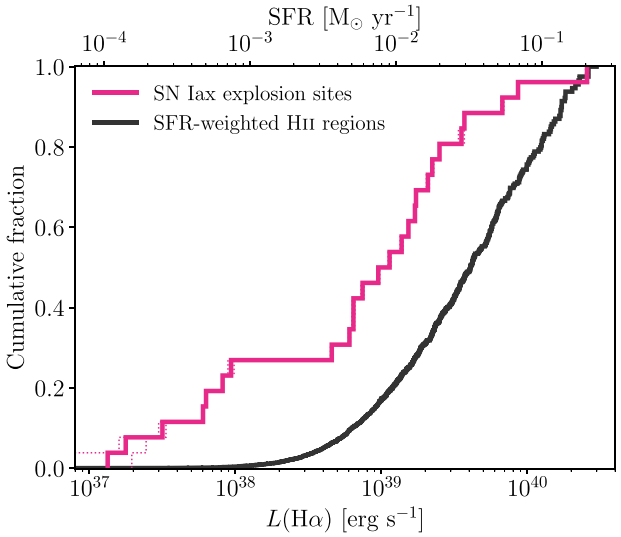

Figure 10. As for Fig. 7 but here showing L(H α) of SN Iax explosion sites. The top axis indicates the corresponding SFR (Kennicutt 1998).

initially very high EW values tend to drop off quickly and largely independent of model differences and reasonable gas parameters.

As an additional check for the presence of very young SPs at the location of SNe Iax, we also attempted fitting for He I λ4922 in our emission fitting routine (Section 3.3) for the MUSE sample.[13] He I λ4922 in emission is present only for ages up to a few Myr (e.g. González Delgado, Leitherer & Heckman 1999). We did not detect this line at any SN Iax explosion site. Within our MUSE data, we found detections of He I λ4922 within 3 kpc of the SN for SNe 2008ha, 2009J, 2010ae, 2012Z and 2013gr. Assuming a 5 Myr age for the young SP (also consistent with EW(H α) $\gtrsim$ 100 found in these regions), the average velocities of the SN Iax progenitors would have to have been in excess of 234, 128, 269, 580, 159 km s^{-1}, respectively, in order to have originated from these regions.

Two events with higher EW(H α) measurements at their explosion sites are debated members of the SN Iax sample as they displayed helium and perhaps hydrogen in their spectra. The removal of these events (SNe 2004cs and 2007J) would lean the typical ages of the young SPs at the locations of the rest of the sample slightly higher (Section 6.4).

5.3 Offsets

Offsets of SNe Iax and H II regions are shown for kpc and host-normalized values in Fig. 11. SNe Iax appear to trace a similar offset distribution as the overall SF of their hosts when accounting for the varying sizes of the host galaxies, although shifted systematically to slightly larger offsets. Since the outer regions of late-type galaxies are likely to be more metal poor and less intensely star forming, this may be a contributing factor to the difference we observe in our other measurements.

[13] Our comparatively shallower NOT data with lower spectral resolution is not conducive to providing meaningful detections of this faint line, which is close to other, much stronger features.

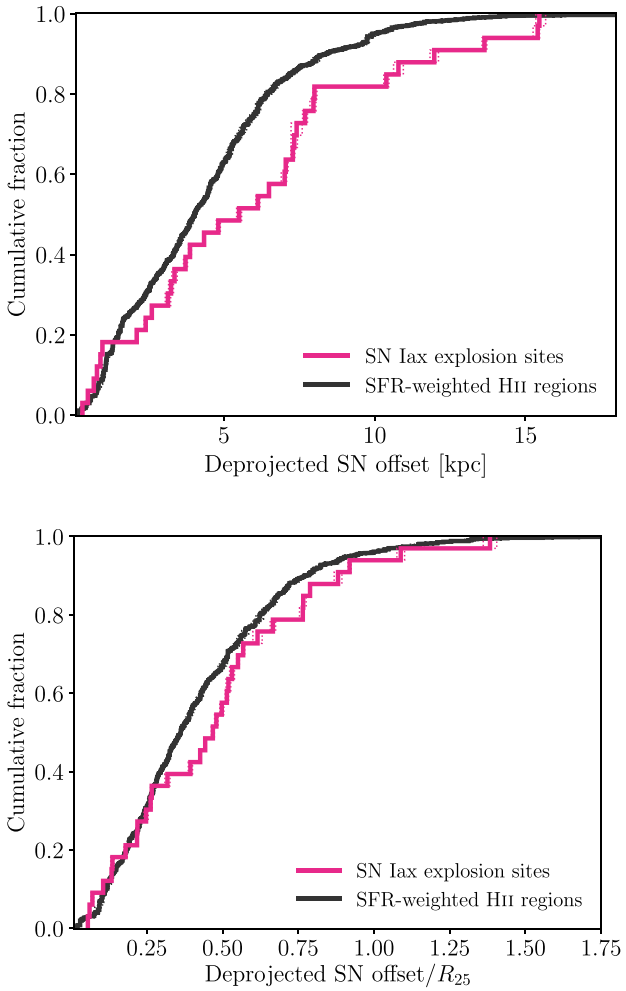

Figure 11. As for Fig. 7 but here showing the deprojected galactocentric offsets of SN Iax explosion sites. The offsets are given in kpc and normalized to the host galaxies' R_{25} values in the top and bottom panels, respectively.

6 DISCUSSION

6.1 Correlation between environment and SN properties

Tying the diversity of progenitor systems to the observed properties of SNe is an open issue amongst all SN types. It may be expected that some imprint of the nature of the progenitor (which can be determined via direct detection or, as here, inferred through environmental analysis) is evident in the SN light curve and spectra.

To investigate this for SNe Iax we plot SN properties, where they have been measured in the literature, against our environmental measures in Fig. 12. The light-curve peak ($M_{\rm peak}$) and decline rate (Δm_{15}) in R or r band, as well as an estimate of the photospheric velocity around peak light ($v_{\rm ph}$) are shown versus the D16 metallicity, EW(Hα) and the host-normalized offsets. Values and references for SN properties are provided in Table 6. In order to expand our comparison sample of SN properties, we include preliminary analyses for SNe 2010el, 2013gr and 2014ey (Stritzinger et al., in preparation)[14] – these objects are to be the subject of more detailed studies in preparation, but our values here are representative.

From these plots, we see that brighter ($M_R \lesssim -16$ mag) members appear to cover almost the full range of the metallicity, EW and offset distributions as found for the full sample, with large spreads in each parameter. Although we have fewer fainter members with peak absolute peak magnitude determinations, we find none at large galactocentric offsets. This trend with galactocentric offset cannot be attributed to observational biases as these work in the opposite direction (very faint transients are more difficult to detect in the brighter central regions of galaxies) and so may actually be more pronounced than is shown. The faint members appear to cluster at a very small range in EW(Hα) of ∼25–40 Å, perhaps indicating more strict age constraints for these members, assuming they arise from the local young SPs. Their metallicities appear diverse although most appear quite metal poor.[15]

Evidence has been presented for a relation between M_R and Δm_{15} for SNe Iax, but any relation is certainly less tight than that seen for normal SNe Ia and with notable outliers (e.g. McClelland et al. 2010; Narayan et al. 2011; Foley et al. 2013). The slowly fading ($\Delta m_{15} \lesssim 0.75$ mag) members of our sample occupy a wide range of environments, with the faster declining members generally occupying more restricted ranges, analogous to the trends seen for the bright and faint members. In particular we observe distinct clustering in metallicity with Δm_{15} – slowly declining members are systematically more metal-rich than the faster decliners (barring the fast declining, metal-rich SN 2010el). A composite figure showing the M_R and Δm_{15} parameter space for SNe Iax now coded by the explosion-site metallicity is shown in Fig. 13. SN 2004cs (based on unfiltered imaging) was a fast declining member although somewhat brighter than the other fast decliners in this plot, and shows a significantly larger EW(Hα) than the other fast decliners (or any of the sample for which we have light-curve information). This was one of two proposed SN Iax members that showed He features, and is further discussed in Section 6.4.

We do not observe any strong clustering or correlated behaviour between our environmental measures and the estimates of photospheric velocity near peak. We caution here, however, that these values have been determined using a variety of methods (spectral synthesis, line measurements based on differing elements) at slightly varying epochs around maximum light, and there thus may be some systematics within the sample. We assign 1000 km s^{-1} uncertainties when plotting, which are likely to be overestimates for individual measurements but account better for potential systematics arising from differing methods.

6.2 SNe Iax environments in the context of other transients

Despite sharing some similarities to SNe Ia in the general spectral classification sense, the host galaxies of SN Iax are almost exclusively (barring SN 2008ge) late type and star forming (e.g. Perets et al. 2010; Foley et al. 2013) and the transients appear to be associated with regions of ongoing SF (this work; Lyman et al. 2013). This is the case for CCSNe and thus a comparison between our results here and those of other SN types in the literature can inform on similarities or differences in the progenitor environments. We

[14] For the three SNe, we find $M_{\rm peak,\,r} \simeq [-15.4, -15.2, -18.1]$ mag, $\Delta m_{15,\,r} \simeq [1.08, 0.99, 0.62]$ mag and $v_{\rm ph} \simeq [3000, 5300, 5000]$ km s^{-1}, respectively. For SN 2010el, we assign an uncertainty of 0.5 mag on the peak owing to the quite uncertain distance to NGC 1566.

[15] For another member, SN 2007qd, McClelland et al. (2010) find a faint peak magnitude ($M_R \simeq -15.8$ mag), although this is uncertain since the light curve does not have full coverage (Foley et al. 2013). We note for this event we only have a poorly constrained (two regions) metallicity gradient from which to estimate the D16 abundance as 8.60.

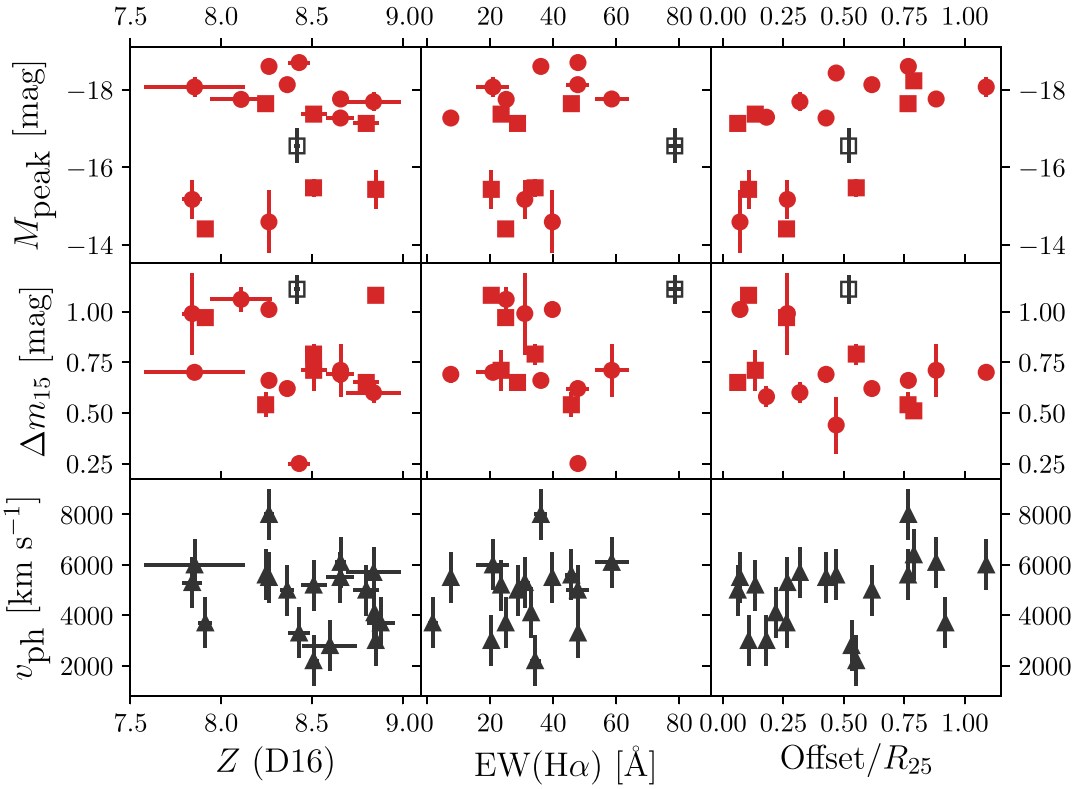

Figure 12. The properties of SNe Iax and their environments. $M_{\rm peak}$ and Δm_{15} values are given in the *R* band (red squares), *r* band (red circles) or unfiltered (for SN 2004cs, empty squares). $v_{\rm ph}$ values are estimates of the photospheric velocity.

Table 6. Values for literature SN properties.

SN name	Filter	Δm_{15}	$M_{\rm peak}$	$v_{\rm ph}$	Reference
2002cx	*R*	0.54 ± 0.06	−17.64 ± 0.15	5600	Foley et al. (2013)
2003gq	*R*	0.71 ± 0.10	−17.37 ± 0.15	5200	Foley et al. (2013)
2004cs	*R*	1.11 ± 0.07	−16.55 ± 0.45	–	Magee et al. (2016)
2005cc	*R*	0.65 ± 0.01	−17.13 ± 0.15	5000	Foley et al. (2013)
2005hk	*r*	0.70 ± 0.02	−18.07 ± 0.25	6000	Stritzinger et al. (2015)
2007qd	–	–	–	2800	Foley et al. (2013)
2008A	*R*	0.51 ± 0.01	−18.23 ± 0.15	6400	Foley et al. (2013)
2008ae	*r*	0.71 ± 0.13	−17.76 ± 0.16	6100	Foley et al. (2013)
2008ha	*R*	0.97 ± 0.02	−14.41 ± 0.15	3700	Foley et al. (2010b)
2009J	*R*	0.79 ± 0.05	−15.47 ± 0.22	2200	Foley et al. (2013)
2009ku	*r*	0.25 ± 0.03	−18.70 ± 0.15	3300	Foley et al. (2013)
2010ae	*r*	1.01 ± 0.03	−14.59 ± 0.81	5500	Stritzinger et al. (2014)
2010el	*R*	1.08 ± 0.03	−15.43 ± 0.50	3000	This work
2011ay	*r*	0.44 ± 0.14	−18.43 ± 0.19	5600	Foley et al. (2013)
2012Z	*r*	0.66 ± 0.02	−18.60 ± 0.09	8000	Stritzinger et al. (2015)
PS1-12bwh	*r*	0.60 ± 0.05	−17.69 ± 0.24	5700	Magee et al. (2017)
2013gr	*r*	0.99 ± 0.20	−15.17 ± 0.50	5300	This work
2014ck	*r*	0.58 ± 0.05	−17.29 ± 0.15	3000	Tomasella et al. (2016)
2014dt	–	–	–	4100[a]	Foley (2015)
2014ey	*r*	0.62 ± 0.02	−18.13 ± 0.10	5000	This work
2015H	*r*	0.69 ± 0.04	−17.27 ± 0.07	5500	Magee et al. (2016)
PS 15csd	*r*	1.06 ± 0.06	−17.75 ± 0.06	–	Magee et al. (2016)

Note. [a]Based on a similarity to SN 2002cx post-peak.

additionally compare to a sample of normal SNe Ia and SN 1991T-like events to compare to two SN classes with expected thermonuclear origins. There are also other peculiar, faint and potentially thermonuclear classes of SNe, such as SN 1991bg-like and Ca-rich events. However, their host galaxy distributions and environments strongly favour very old progenitors (e.g. van den Bergh, Li & Filippenko 2005; Perets et al. 2010; Lyman et al. 2016; Lunnan et al. 2017), in stark contrast to SNe Iax. (A direct comparison

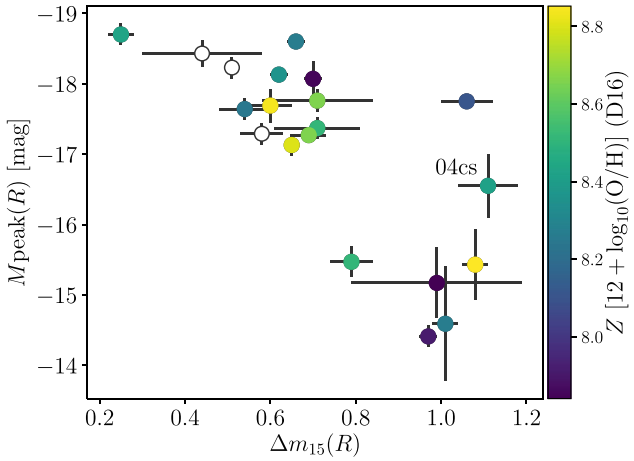

Figure 13. *R*- and *r*-band $M_{\rm peak}$ versus Δm_{15} for SNe Iax (e.g. Narayan et al. 2011; Foley et al. 2013; White et al. 2015; Tomasella et al. 2016) in our sample, now colour coded by their environmentally derived metallicities in the indicator of D16 where possible. SN 2004cs is highlighted as the classification of this event is debated (Section 6.4).

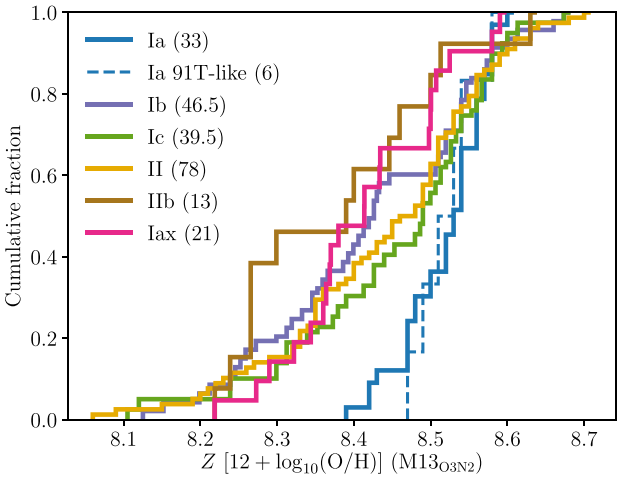

Figure 14. The explosion-site metallicity distributions of SNe Iax compared to literature samples of other principal SN types. Metallicities are based on the O3N2 indicator of M13.

between the environments of Ca-rich SNe and SNe Iax was presented in Lyman et al. 2013.)

The construction of our comparison SN samples does not constitute unbiased, blindly targeted events by any means. However, the same holds for the SN Iax sample, which were discovered over a variety of surveys. Our comparison is thus limited to an initial, indicative comparison until such time as a reasonable sample of homogeneously discovered SNe Iax exists.

6.2.1 *Metallicity*

As we are working with literature samples, there are almost no abundance measurements in the D16 scale owing to its recent inclusion in the literature. We therefore collect available values based on the O3N2 indicator (these were generally presented in the calibrations of Pettini & Pagel 2004 and have been translated to those of M13). We used only values based at or nearby the SN explosion site, or based on determined gradient values (i.e. we exclude those where the metallicity was determined based on the host nucleus but the SN was at a significant offset and not covered by the slit/fibre).

We take values from the analyses of Anderson et al. (2010), Modjaz et al. (2011), Leloudas et al. (2011), Sanders et al. (2012), Kuncarayakti et al. (2013a), Kuncarayakti et al. (2013b), Stoll et al. (2013) and Galbany et al. (2016a). In the case of SNe II (including both II-L and II-P), we take values from Anderson et al. (2016, which includes the results of Anderson et al. 2010) and Galbany et al. (2016a) directly in M13, and values from Stoll et al. (2013). On the values of Anderson et al. (2016), we impose a distance cut of 3 kpc on the H II region – SN distance. We present SNe Ib and Ic separately; however, uncertain classifications mean there is likely to be some cross-contamination. Where appropriate we use the updated classifications of Modjaz et al. (2014) and Shivvers et al. (2017) and count still uncertain 'Ib/c' designations with half weight in each cumulative distribution. SNe Ia 91T-like events were taken from Galbany et al. (2016a) but with updated values to be presented in the PMAS/PPAK Integral-field Supernova hosts COmpilation (PISCO; Galbany et al. in preparation).

We plot the explosion-site metallicity distributions for SNe Iax and our comparison samples in Fig. 14. There is no significant difference between SNe Iax explosion-site metallicities and those of SNe Ib, Ic, II or IIb and the median value for SNe Iax (8.41 dex) is close to that of the others (Ib: 8.42 dex, Ic: 8.49 dex, II: 8.47 dex, IIb: 8.39 dex). The distribution for SNe Iax covers broadly the same range as these other SN types, perhaps not extending as metal rich or poor as SNe Ib, Ic or II; however, there are only a very small number of events in these samples on the extreme edges of their distributions. Compared to the SNe Ia distribution (local metallicity measurements explosion sites from IFS data taken from Galbany et al. 2016a), with median 8.53 dex, we see SNe Iax are metal poor (KS test Ia versus Iax metallicities $p = 5 \times 10^{-4}$). Although we are limited in sample size, the SN 1991T-like events also appear at relatively high metallicities, tracing the SN Ia distribution well, with a corresponding lack of low-metallicity events, cf. SNe Iax. The median metallicity of SN 1991T-like events is 8.52 dex. A KS test between these and the SN Iax sample gives $p = 0.016$ that they are drawn from the same distribution. Thus, although the host galaxy type distributions of SN 1991T-like events are similar to those of SNe Iax (Perets et al. 2010), the results here suggest that their environmental metallicities are different.[16]

Although the overall SN Iax distribution appears to follow broadly the distributions of other well-known SN types, barring SNe Ia, it is overall quite different from the distribution of low-redshift LGRB explosion sites, which are in the range $Z_{\rm O3N2} \simeq$ 8.0–8.4 dex (e.g. Modjaz et al. 2008; Sanders et al. 2012). Similar very low metallicities have also been found for the vast majority of superluminous supernova hosts (e.g. Lunnan et al. 2014; Leloudas et al. 2015).

6.2.2 *Offsets*

R_{25}-normalized offset distributions for SNe Ib, Ic, II and IIb were taken from Taddia et al. (2013). SNe Ia offsets were taken from the

[16] The D16 metallicities of the SN 1991T-like events are $Z = 8.5$–8.9 dex (Galbany et al., in preparation), showing a lack of low-metallicity events cf. the SN Iax distribution (Fig. 7) for this indicator also.

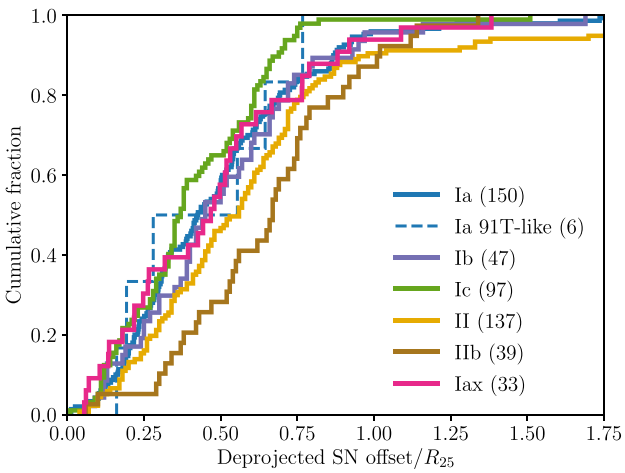

Figure 15. The explosion-site galactocentric offset distributions of SNe Iax compared to literature samples of other well-known SN types. Offsets have been normalized by their hosts' respective R_{25} values.

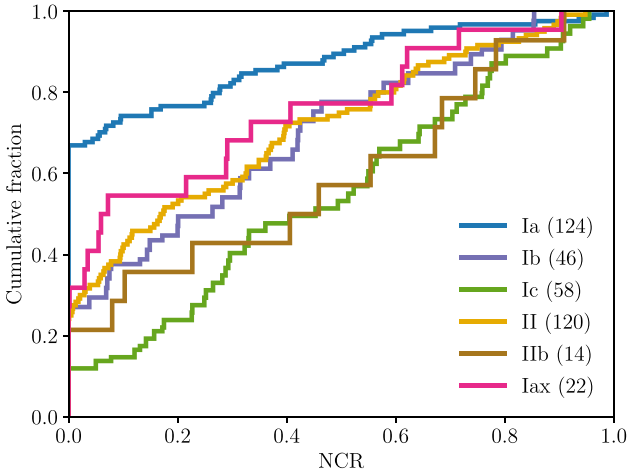

Figure 16. The explosion-site NCR distributions of SNe Iax compared to literature samples of other well-known SN types. NCR values were calculated using Hα maps from our MUSE data cubes and supplemented with values presented in Lyman et al. (2013).

catalogue of Hakobyan et al. (2016) and calculated following the prescription described therein. The SNe Ia host-normalization are based on g-band R_{25} measurements as opposed to B-band measurements used for the other samples. This may introduce a systematic offset in the values, however, given the considerable filter overlap and the modest variation of apparent galaxy sizes around these wavelength ranges (Vulcani et al. 2014), the effect is likely to be small. SNe Ia in the catalogue are those that exploded in disc galaxies (types S0-Sm). SN 1991T-like offsets were taken from Galbany et al. (2016a) and then normalized to the host R_{25} values from NED.

Similarly to the metallicities, we see in Fig. 15 that the offsets of SNe Iax closely match other SNe types, in particular SNe Ia and Ib. Offsets do not appear to be a strong factor in distinguishing SNe Iax, whereas their host galaxy type distribution proves more discriminatory against that seen for SNe Ia (Perets et al. 2010; Lyman et al. 2013).

6.2.3 *Pixel statistics*

An analysis of the NCR (Section 3.3.5) distribution of SNe Iax was presented by Lyman et al. (2013), who found the association of SNe Iax to SF in their hosts was at a similar level to that of SNe IIP and inferred similar progenitor ages (tens of Myr). As we are able to create Hα maps from our MUSE data cubes, we present an updated comparison figure with this extended combined sample of SNe Iax in Fig. 16. Other SN sample data are taken from Anderson & James (2008) and Anderson et al. (2012, 2015) and, following Lyman et al. (2013), we have corrected the SN Ia sample to account for the fact that only late-type galaxy hosts were used but ∼27 per cent of SNe Ia explode in early-type hosts (Li et al. 2011), with no appreciable ongoing SF. For SNe 2005P, 2008ha, 2009J and 2012Z, we use values from Lyman et al. (2013) as Hα imaging presented there covers the full spatial extent of the hosts. The NCR values for these determined in Lyman et al. (2013) and here are [0.06, 0.41, 0.00, 0.00] and [0.01, 0.33, 0.06, 0.03], respectively. No NCR values for SN 1991T-like events are currently available in the literature; however, a preliminary analysis, to be presented in Barnsley et al. (in preparation), indicates their mean NCR is 0.22 ± 0.06 (standard error on mean), close to that of SNe Iax: 0.24 ± 0.06.

Following Lyman et al. (2013), we confirm for a larger sample that SNe Iax display a level of association with the SF of their hosts most similar to that of SNe II. Their distribution is formally discrepant, based on the KS test, with the SNe Ia and Ic distributions at 3σ (considering only SNe Ia in late-type hosts and excluding SN 2008ge from the SN Iax sample, the SN Ia versus Iax discrepancy is $p = 0.05$).[17] Although there are few Hα NCR values for LGRBs (due to their typically much larger distances), studies have shown these to be very strongly associated with the brightest SF regions of their hosts, at a level exceeding SNe Ic (Fruchter et al. 2006; Svensson et al. 2010; Lyman et al. 2017). Assuming the same would hold for SF as traced by Hα, this infers drastically different environments of SNe Iax compared to LGRBs.

We note that although we detected Hα at the locations of all our SNe Iax in the MUSE sample, we have somewhere NCR = 0.00. In order to facilitate comparison to literature samples, which were performed using narrow-band imaging, we construct Hα narrow band images (filter width 30 Å) and subtract the neighbouring continuum within our data cubes (Section 3.1.1). As such, very faint sources of emission may become dominated by shot noise or inaccuracies in continuum subtraction during the Hα map construction, leaving the pixel within the noise floor of the image (defined as NCR = 0, see James & Anderson 2006; Anderson & James 2008, for more thorough discussion). Additionally, the spatial extent of our spaxel bins is larger than the 3 × 3 binning employed for the NCR calculations in order to replicate the method used in the literature.

6.3 Ionized gas in the early-type host of SN 2008ge

Although there are likely to be contributions from different progenitor channels to such a diverse class of objects (see Section 6.4), one SN in the Iax sample has been marked out by its unique environment and host. SN 2008ge was hosted by NGC 1527, an early, weakly barred S0 galaxy (de Vaucouleurs et al. 1991), in contrast to the strongly star-forming, late-type hosts of other known Iax

[17] Anderson–Darling tests provided very similar levels of significance, with slightly higher significance for the uncorrected SNe Ia versus Iax ($p \simeq 0.006$).

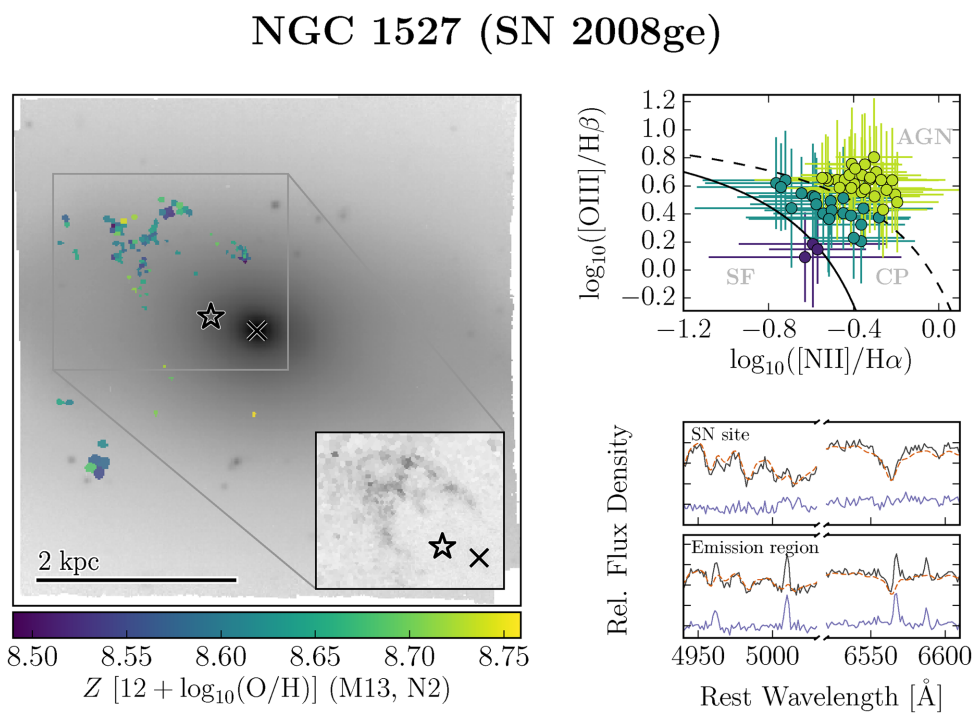

Figure 17. The central ionized gas component of NGC 1527 (the host of SN 2008ge). *Left:* a heatmap of the metallicity (using the N2 relation of M13) for each bin where both H α and [N II] λ6583 has SNR > 2, overlaid on an inverted *R*-band image of the galaxy; north is up, east is left. The adopted location of the nucleus and the SN explosion site are indicated by the black $\times$ and 'star' symbols, respectively. *Left, inset:* an inverted, continuum-subtracted [O III] image of the central region of NGC 1527. Each Voronoi bin has had its best-fitting stellar continuum model (Section 3.2) subtracted. The residual ionized gas component is evident *Top right:* a BPT diagram for those bins with detected emission. The format is the same as shown in Fig. 2. *Bottom right:* the observed spectrum (black) with the STARLIGHT fit to the continuum (orange, dashed) and the residual emission (purple) around H α and [N II]. This is shown for the SN explosion site, where we do not detect any significant emission lines, and in one of the bins NE of the galaxy nucleus, from which we were able to measure a metallicity. Wavelengths are in the rest frame of the nucleus of NGC 1527.

(Perets et al. 2010; Lyman et al. 2013). Motivated by this, Foley et al. (2010a) investigated the host galaxy and explosion site for signs of a young SP. They concluded from a smooth galaxy profile, non-detection of far-infrared or H I 21cm emission in the host, and the lack of narrow nebular emission lines in their host galaxy spectrum that there is no significant ongoing SF (and thus young SPs) in NGC 1527.

Our MUSE observations provide deep optical spectra, spatially resolved, across a reasonable fraction of the central regions of the host galaxy. After an initial pass with our emission line fitting as presented in Section 3, we reran the emission line fitting this time fitting only for H α and [N II] λ6548,6583 in order to determine a subset of the bins with evidence for ionized emission lines. We then attempted to fit H β and [O III] λ5007 for these bins. In accordance with Foley et al. (2010a), we found no significant emission lines at the location or in the close vicinity of the SN explosion site (either within the Voronoi bin directly underlying the explosion site or by extracting circular apertures of varying sizes). However, within our MUSE data, we detected an ionized gas stream arcing from the NE of the nucleus with evidence for a further region of emission to the SE of the host nucleus. As NGC 1527 is particularly nearby ($\sim$17 Mpc), the MUSE observations only cover the central $\sim$2–3 kpc around the nucleus. We have summed the H α flux captured by the MUSE FOV and determine $\log_{10}(L(\mathrm{H}\,\alpha) = 37.6\,\mathrm{erg\,s^{-1}}$ and note that this is not corrected for the effects of reddening as we were unable to detect H β in many of the bins. For the case that this emission is driven by ongoing SF, the relation of Kennicutt (1998) suggests the detected emission equates to $\log_{10}(\mathrm{SFR}) = -3.48\,\mathrm{M_\odot\ yr^{-1}}$. This is consistent with the limit that Foley et al. (2010a) provide for NGC 1527 of $\log_{10}(\mathrm{SFR}) < -2.14\,\mathrm{M_\odot\ yr^{-1}}$. The metallicity (for SF-driven ionization) appears to be around solar to slightly subsolar based on the N2 indicator (M13). The EW(H α) of the bins are $\sim$0.8 Å.

Morphologically the main stream appears somewhat coherent, in a thin parabolic stream about the nucleus. The emission looks different to the more extended, and generally more symmetric, spiral arms seen in some early-type galaxies (ETGs; see Gomes et al. 2016a, and references therein). The nature of the ionizing sources in ETGs is debated and there appears to be contributions from a variety of phenomena, with different mechanisms dominating in different galaxies (e.g. Goudfrooij 1999; Sarzi et al. 2006, 2010). Unfortunately, we are limited in our analysis for the ionizing source based on emission line flux ratios as we are close to our detection limits and thus flux ratios are not well constrained. Within Fig. 17, we plot the BPT diagram for bins where all lines were detected at SNR > 1. Although the position of each bin is rather uncertain within this diagram, there appears to be a general clustering of the bins around or above the maximal SF relation of Kewley et al. (2001), indicative that ongoing SF may not be the dominant process driving this emission. (Those bins that are more consistent with being ionized solely due young, massive stars are those SE of the nucleus, not in the main arc.) With a comparison to the study of Sarzi et al. (2010), the stronger line ratios and morphology may be more reminiscent of emission due to shocks in the galaxy, although these are not

expected to be dominating sources of ionization in ETGs. Alternatively it may be due to diffuse ionizing SPs, such as post-asymptotic giant branch (pAGB) stars.

The ionizing flux from pAGB stars can lead to line ratios similar to those seen for low-ionization emission-line regions (LIERs; Binette et al. 1994; Sarzi et al. 2006), and the bulk of the bins in Fig. 17 are located close to LIER areas of the parameter space (e.g. $\log_{10} \frac{[\mathrm{N\,II}]\lambda6583}{\mathrm{H}\alpha} \gtrsim -0.4$ and EW(H α) < 6 Å; Cid Fernandes et al. 2011). One would, however, expect a pAGB population to be more or less pervasive across the galaxy and follow the distribution of stellar mass. This results in the correlation between ionized line flux and stellar continuum flux seen in ETGs with pAGB ionizing sources (Sarzi et al. 2010). A more structured ionized region (as seen here) could therefore be due to variations in gas column density within the galaxy. The ionizing output and subsequent EW(H α) predictions from various models for pAGB star contributions predict roughly constant low values from $\sim 10^8$ to $10^{9.5}$ yr (Cid Fernandes et al. 2011), meaning such values do not offer strong constraints on the relative age of the underlying population.

6.4 Heterogeneity of the class and contaminants

As is the case for many astrophysical transients, in particular for peculiar and relatively rare objects, membership to a particular class (or even designating a single class) can be contentious. Often the underlying continua of the event properties are at odds with defining distinct regions of parameter space to assign one class or another. This is exemplified in the case of SNe Iax, where multiple progenitor channels and explosion mechanisms may be contributing to empirically similar transients.

Two examples in the sample of Foley et al. (2013) showed evidence for helium in their spectra: SNe 2004cs and 2007J. Helium can remain hidden in SN spectra as it is difficult to ionize and so it is possible that helium is present in the ejecta of other members; however, at the time of writing these two members remain the only posited SNe Iax to show detections. One potential confusion, as highlighted by Foley et al. (2013), is with SN 2005E-like events (Perets et al. 2010, also known as Ca-rich transients/SNe) – these similarly faint-and-fast events display helium features in their spectra before quickly evolving to unusually Ca-dominated nebular spectra (Kasliwal et al. 2012). Instead, White et al. (2015) favour the original classifications of SNe 2004cs and 2007J as CC-SNe. In addition to helium, they also find evidence for hydrogen in their spectra, prompting classifications of SNe IIb. However, a re-analysis by Foley et al. (2016) argued against the presence of hydrogen in SN 2007J, citing an identification as [Fe II] of the same feature in SN 2002cx. Furthermore, they find inconsistencies between the light curve of SN 2004cs and other known SNe IIb. As we are discussing only two objects, statistical inferences from environmental measures are weak. This is further exacerbated by the fact that our measures overlap significantly for SNe Iax and SNe IIb (Section 6.2). For completeness, we note EW values at the helium-SNe Iax explosion sites are among the highest (first and fourth) of our sample, pointing to the presence of younger SPs at their explosion sites than typical SNe Iax. Their offsets ($\simeq 0.5 \times R_{25}$) and metallicities (O3N2 $\simeq$ 8.4) are typical of the samples of both SNe Iax and IIb. Their exclusion would revise our estimates of the typical ages of the young SP at SN Iax explosion sites slightly higher, although the quantitative effect is likely to be dwarfed by the inherent uncertainties present in determining ages from nebular gas spectra (Stanway et al. 2014, Section 3.3.4), and would not significantly affect our discussion elsewhere.

SN 1999ax was classified as a 'somewhat peculiar' SN Ia by Gal-Yam et al. (2008) at $z \simeq 0.05$. On the basis of SDSS spectra of a nearby potential host showing it to be at $z = 0.023$, Foley et al. (2013) re-analysed its spectrum and classified it as an SN Iax based on similarity to SN 2002cx post-peak. We note our NOT spectroscopy of the explosion site also covered another nearby object in SDSS that is at a similar (projected) offset from SN 1999ax as the galaxy at $z = 0.023$ (with the SN being located between the two). We find this galaxy is at $z = 0.059$ based on the H α line in the NOT spectrum. As the SN is located directly between the two potential hosts, it is difficult to distinguish the likely host from environments alone. The velocities of the features in the spectrum appear low compared to normal SN Ia, and a consideration of the SN at $z \simeq 0.05$ still poses peculiarities to a typical SN Ia classification, as such we retain the SN Iax classification making the lower redshift galaxy the probable host.

6.5 Implications for progenitor models

Pure deflagrations (e.g. Branch et al. 2004; Jha et al. 2006; Phillips et al. 2007; Jordan et al. 2012; Kromer et al. 2013; Fink et al. 2014; Magee et al. 2016), pulsational-delayed detonations (Stritzinger et al. 2015) and helium-ignition (Wang et al. 2014) of WDs have been presented as progenitor models to explain SNe Iax. Although too weak to account for normal SNe Ia, they broadly agree with the low ^{56}Ni masses and kinetic energies displayed by SNe Iax. There are currently limited predictions as to the progenitor environments for these based on population studies, with the main constraints in the form of delay-time distributions and age constraints.

Any double-degenerate channel (either merger or accretion between two WDs) would require circumstances to explain the young environments since such progenitor systems would be expected to be prevalent in old SPs and ETGs, inconsistent with the locations of SNe Iax as a whole. As such, single-degenerate formation channels are generally favoured for SN Iax.

Meng & Podsiadlowski (2014) found that delay times as low as 30 Myr were possible for massive hybrid CONe WDs accreting material until the Chandrasekhar mass, and would likely produce lower luminosity events (cf. normal SNe Ia) making them an attractive possibility for SNe Iax. Wang et al. (2013) explore detonation of CO WDs via ignition in a helium envelope that is accreted from an He companion. For the case of a non-degenerate companion their delay times to explosion are $\sim 10^8$ yr, consistent with the ages of young SPs at the location of most SNe Iax. If the companion is an He WD, the delay time can be significantly extended (up to the Hubble time), potentially providing an explanation for SNe Iax in old populations (e.g. SN 2008ge) or those with no detected signs of SF at the explosion site and in the outskirts of their hosts (e.g. SN 2008A). We note that these are for solar metallicity populations, which is metal-rich compared to the SN Iax population (Fig. 7). Similarly, Liu et al. (2015b) find that the WD + He star channel best reproduces the young ages of SN Iax explosion sites, but note an extended delay time exists for main sequence or red giant companions. Our age constraints on SNe Iax seem to be in good agreement with predictions of young explosion scenarios of single-degenerate thermonuclear progenitor models.

6.5.1 *Faint and fast 'SN 2008ha-like events'*

The faintest, lowest energy members of SNe Iax could represent a distinct population of events, with the most famous example being

SN 2008ha (see Foley et al. 2009, for further discussion of models in light of the physical properties of the SNe). These very faint examples are difficult to produce with models proposed for other SNe Iax (Fink et al. 2014), perhaps indicating a single model is not able to explain the full diversity of all events labelled as such. For the purposes of this section, we simply refer to faint ($M_R > -16$ mag) and (/or) fast evolving ($\Delta m_{15} \gtrsim 1$ mag) members of the sample, ignoring a detailed spectroscopic distinction.

Valenti et al. (2009) suggested SN 2008ha and, by extension, other SNe Iax were of core-collapse origin. Our environmental analyses indicate that the fainter members arise from low-metallicity regions, quite centrally located on their host galaxies (Fig. 12). From an environmental viewpoint, their distributions are largely consistent with those seen for well-known CCSN types. The question of whether they are due to lower mass, $\sim$8 $M_\odot$, stars stripped of their hydrogen envelopes or very massive WR stars, probable progenitors of LGRBs, experiencing significant fallback, was posed by Valenti et al. (2009). Our analysis of the ages of the youngest SPs here suggests ages of order tens of Myr for their explosion sites (Section 5.2). This is in agreement with resolved SP studies of explosion sites of nearby SNe Iax (Foley et al. 2014; McCully et al. 2014a) and the comparative association of SNe Iax to Hα emission in their host galaxies at the level of SNe II (Section 6.2.3; Lyman et al. 2013). For WR stars, however, we may expect much younger ages, $\lesssim$10 Myr (for stars with initial masses of $\gtrsim$25 $M_\odot$). Consequently, we would expect larger EW values at the explosion sites (e.g. see the low-redshift LGRB environment studies of Christensen et al. 2008; Thöne et al. 2008; Izzo et al. 2017; Krühler et al. 2017), and an association with ongoing SF of their hosts at a level much higher than is seen for SNe Iax (Section 6.2.3, see also Kangas et al. 2017).

A search for He I λ4922 in emission (indicative of SPs of only a few Myr) in the hosts of our MUSE sample found 5 SNe Iax with such young regions within 3 kpc. This include four of the five events with peak luminosities known to be ≥ -16 mag plus SN 2012Z (the missing low-luminosity event is SN 2010el). The host galaxies of these fainter members are typically more irregular and exhibit signatures of extremely young SPs within them, with EW(Hα) reaching hundreds of Å. In order to establish a causal link between the SNe and their nearest very young regions, progenitor velocities of hundreds of km s^{-1} must be invoked (Section 5.2). To produce such high-mass and velocity runaways requires very rare dynamical ejections or unfeasibly large ejection velocities after a binary companion goes SN (Eldridge, Langer & Tout 2011, see also discussion in Krühler et al. 2017). Our results would therefore disfavour the very massive progenitor scenario (for the SN Iax sample as a whole and the SN 2008ha subset). Moriya et al. (2010) concur, finding that their 25 and 40 $M_\odot$ fallback models cannot reproduce the observations of SN 2008ha, but find better agreement with a 13 $M_\odot$ model.

Deflagrations of hybrid CONe have been proposed to explain the weak SN 2008ha by Kromer et al. (2015). Although occurring in Chandrasekhar-mass WDs, the deflagration is not propagated into the outer ONe layer, which results instead in lower energy release and consequently low ejecta masses (cf. CO WD explosions), leaving behind a bound remnant. The ejecta mass in the model is below estimates for SN 2008ha, resulting in too quickly rising and fading light curves, and also affecting the spectral comparison. The delay time to explosion for CONe WDs with helium donor stars has been estimated at $\sim$few $\times$ 10^7–10^8 yr by Wang et al. (2014) and Kromer et al. (2015), albeit at solar metallicity that may not be representative of the typical environments of SN 2008ha-like events. This is in agreement with this study and Foley et al. (2014).

Moriya & Eldridge (2016) present an initial study of the light curves and rates for binary evolution channels of SE-EC SNe, which may have relation to the low-luminosity CCSN scenario of Valenti et al. (2009). They find broad agreement with SN 2008ha-like events in terms of peak magnitude and their rapidly evolving light curves, and that the rates of SE-EC SNe are significantly enhanced at low metallicities. For our five events peaking at $M_R > -16$ mag, we determined a wide spread of metallicities (see also Foley et al. 2009; Stritzinger et al. 2014), including very low metallicity events and the quite metal-rich SN 2010el. In the case of the rapidly declining events (note that these are not all overlapping with the faint events, e.g. PS 15csd; Magee et al. 2016), we similarly find low metallicities for all but SN 2010el. SE-EC SNe progenitors are expected to come from the lower end of the mass range of massive SNe progenitors $\sim$7–8 $M_\odot$ and we therefore expect to see evidence for young, but not exceptionally young SPs at their explosion sites – this is borne out in the relatively modest EW(Hα) values we find of 25–40 Å. We therefore confirm here the preference for faint and/or fast subsets of SNe Iax (SN 2008ha-like events) to be preferentially in lower metallicity environments with signatures of relatively young SPs at their explosion sites, consistent with current predictions for SE-EC SNe by Moriya & Eldridge (2016, see also Pumo et al. 2009). In this scenario, the proposed donor or remnant of SN 2008ha (Foley et al. 2014) would be the companion star that may have stripped the envelope of the SN progenitor. The spectral predictions for SE-EC SNe that are needed to provide a full comparison to SN 2008ha-like events are currently lacking.

7 CONCLUSIONS

We have presented a spectroscopic survey of the explosion sites and host galaxies of SNe Iax and fitted emission line regions in our VLT/MUSE IFS and NOT/ALFOSC long-slit observations.

We determined deprojected metallicity gradients for all hosts where possible and found that estimates of the explosion sites' metallicities based on these gradients agreed well with our direct measurements. With this our explosion-site metallicity sample was supplemented with gradient estimates where we could not measure the location directly. The majority of SN Iax explosion sites were found to be subsolar ($12 + \log_{10}(\mathrm{O/H}) \simeq 7.75$–$8.85$ dex in the scale of D16), and generally metal poor compared to the distribution of SF in their hosts (Section 5.1).

SNe Iax explosion sites appeared to be less intensely star forming and somewhat older than the typical SF region of the hosts (Section 5.2), although they do follow a similar host-normalized offset distribution (Section 5.3). Through comparison with a fiducial gas model and the results of the SP synthesis code BPASS, we estimate the ages of the young SPs at the explosion sites of SNe Iax to be several $\times$ 10^7 to 10^8 yr old (although note the caveats on assigning quantitative values in Section 3.3.4). The relatively young ages at the explosion sites are confirmed through a similarity in their association with the ongoing SF of their host galaxies to that seen for SNe II (Section 6.2.3), which are expected to have typical ages of tens of Myr, extending up to $\simeq 10^8$ yr (Zapartas et al. 2017).

Assessing our environmental measures in terms of SN properties, we find that the brighter, more slowly fading objects define our range of metallicities, EW(Hα) and offsets by covering the entire ranges (Section 6.2). Faint and faster events appear to occupy more restricted ranges of EW values and host offsets, although we are limited to only a few objects for which we can investigate. Their

metallicities extend across a wide range including some of the most metal poor and metal rich in the whole sample. We find no correlations between the velocity of the SNe and our environmental parameters. The only two designated SNe Iax to display helium (SNe 2004cs, 2007J) have among the highest EW(Hα) values of the sample, indicate the presence of comparatively younger SPs. Their membership as SNe Iax has been debated (White et al. 2015; Foley et al. 2016). With just two events, we are limited in searching for statistical difference between these and the rest of the SNe Iax and their environments appear typical of both SNe Iax and IIb (the suggested typing of White et al. 2015).

When compared to other SN types, SNe Iax as a whole display a similar metallicity distribution to that seen for SNe Ib/c and II, with similar median values and covering a broadly similar range in metallicity. Their metallicities cover a much larger spread and extended to lower metallicities than those seen for either normal SN Ia or SN 1991T-like events. The host-normalized offset distribution of SNe Iax follows closely that seen for SNe Ia in disc galaxies and SNe Ib. Using pixel statistics, SNe Iax trace the ongoing SF of their hosts at a level most similar to SN II and significantly more so than SNe Ia, but less than SNe Ic (and LGRBs).

For the S0 host of SN 2008ge, NGC 1527, we discover a stream and clumps of ionized gas not seen in previous studies. A limited analysis of emission line ratios would disfavour a SF-driven ionizing flux, with an evolved SP or shocks more likely to be powering it. We find no evidence of ionized gas at, or nearby, the location of SN 2008ge and confirm its environment is old compared to the rest of SNe Iax. The ionized component suggests that there may have been SF in NGC 1527 relatively recently and thus ∼Gyr old progenitors are not required.

The young explosion sites we confirm here remain in good agreement with the expectations for progenitors consisting of CO/CONe WD + He stars and moderately massive CCSNe with fallback or SE-EC SNe. The lack of features associated with very young environments disfavour the presence of very massive stars at the explosion site. We would therefore consider the model of massive WR stars suffering fallback on to a black hole upon collapse as unlikely progenitors (without having to invoke implausibly large runaway velocities), ruling out faint SNe Iax as a way to explain local, apparently SN-less LGRBs.

ACKNOWLEDGEMENTS

The anonymous referee is thanked for their comments and suggestions for the manuscript. We thank Ryan Foley for providing the late-time spectra of SN 2014dt. David Balam is thanked for providing the spectrum of PSN J22412689+3917220 (now SN 2015ce) for its registration on the Transient Name Server. Eric Hsiao and the iPTF collaboration are thanked for their assistance registering PTF 14ans (now SN 2014ey) on to the Transient Name Server. Lise Christensen is thanked for comments on a draft of the manuscript. JDL gratefully acknowledges support from the UK Science and Technology Facilities Council (grant IDs ST/L000733/1 and ST/P000495/1). MDS gratefully acknowledges support provided by the Danish Agency for Science and Technology and Innovation realized through a Sapere Aude Level 2 grant, the VILLUM FONDEN (research grant 3261), and the Instrument Centre for Danish Astrophysics (IDA). Based on observations collected at the European Organisation for Astronomical Research in the Southern Hemisphere under ESO programmes 095.D0091, 096.D-0263 and 099.D-0022. Based on observations made with the Nordic Optical Telescope (proposal numbers 52-004 and P3-005; PI: Stritzinger), operated by the Nordic Optical Telescope Scientific Association at the Observatorio del Roque de los Muchachos, La Palma, Spain, of the Instituto de Astrofisica de Canarias. This research has used the NASA/IPAC Extragalactic Database (NED) which is operated by the Jet Propulsion Laboratory, California Institute of Technology, under contract with the National Aeronautics and Space Administration. We acknowledge the usage of the HyperLeda data base (http://leda.univ-lyon1.fr). This research used ASTROPY, a community-developed core PYTHON package for Astronomy (Astropy Collaboration 2013).

REFERENCES

Andersen D. R., Bershady M. A., 2013, ApJ, 768, 41
Anderson J. P., James P. A., 2008, MNRAS, 390, 1527
Anderson J. P., Covarrubias R. A., James P. A., Hamuy M., Habergham S. M., 2010, MNRAS, 407, 2660
Anderson J. P., Habergham S. M., James P. A., Hamuy M., 2012, MNRAS, 424, 1372
Anderson J. P., James P. A., Habergham S. M., Galbany L., Kuncarayakti H., 2015, PASA, 32, e019
Anderson J. P. et al., 2016, A&A, 589, A110
Asplund M., Grevesse N., Sauval A. J., Scott P., 2009, ARA&A, 47, 481
Astropy Collaboration, 2013, A&A, 558, A33
Bacon R. et al., 2010, in McLean I. S., Ramsay S. K., Takami H., eds, Proc. SPIE Conf Ser. Vol. 7735, Ground-based and Airborne Instrumentation for Astronomy III. SPIE, Bellingham, p. 773508
Balam D. D., Graham M. L., 2015, Astron. Telegram, 7931
Baldwin J. A., Phillips M. M., Terlevich R., 1981, PASP, 93, 5
Binette L., Magris C. G., Stasińska G., Bruzual A. G., 1994, A&A, 292, 13
Branch D., Baron E., Thomas R. C., Kasen D., Li W., Filippenko A. V., 2004, PASP, 116, 903
Bruzual G., Charlot S., 2003, MNRAS, 344, 1000
Cappellari M., Copin Y., 2003, MNRAS, 342, 345
Cardelli J. A., Clayton G. C., Mathis J. S., 1989, ApJ, 345, 245
Chabrier G., 2003, PASP, 115, 763
Childress M. J. et al., 2015, MNRAS, 454, 3816
Christensen L., Vreeswijk P. M., Sollerman J., Thöne C. C., Le Floc'h E., Wiersema K., 2008, A&A, 490, 45
Cid Fernandes R., Mateus A., Sodré L., Stasińska G., Gomes J. M., 2005, MNRAS, 358, 363
Cid Fernandes R., Stasińska G., Mateus A., Vale Asari N., 2011, MNRAS, 413, 1687
de Vaucouleurs G., de Vaucouleurs A., Corwin H. G., Jr, Buta R. J., Paturel G., Fouqué P., 1991, Third Reference Catalogue of Bright Galaxies. Volume I: Explanations and references. Volume II: Data for galaxies between 0^h and 12^h. Volume III: Data for galaxies between 12^h and 24^h. Springer-Verlag, Berlin
Della Valle M. et al., 2006, Nature, 444, 1050
Dopita M. A., Kewley L. J., Sutherland R. S., Nicholls D. C., 2016, Ap&SS, 361, 61 (D16)
Eldridge J. J., Stanway E. R., 2009, MNRAS, 400, 1019
Eldridge J. J., Stanway E. R., 2012, MNRAS, 419, 479
Eldridge J. J., Langer N., Tout C. A., 2011, MNRAS, 414, 3501
Ferland G. J., Korista K. T., Verner D. A., Ferguson J. W., Kingdon J. B., Verner E. M., 1998, PASP, 110, 761
Filippenko A. V., 1997, ARA&A, 35, 309
Filippenko A. V. et al., 1992a, AJ, 104, 1543
Filippenko A. V. et al., 1992b, ApJ, 384, L15
Fink M. et al., 2014, MNRAS, 438, 1762
Foley R. J., 2015, MNRAS, 452, 2463
Foley R. J. et al., 2009, AJ, 138, 376
Foley R. J. et al., 2010a, AJ, 140, 1321
Foley R. J., Brown P. J., Rest A., Challis P. J., Kirshner R. P., Wood-Vasey W. M., 2010b, ApJ, 708, L61

Foley R. J. et al., 2013, ApJ, 767, 57
Foley R. J., McCully C., Jha S. W., Bildsten L., Fong W.-f., Narayan G., Rest A., Stritzinger M. D., 2014, ApJ, 792, 29
Foley R. J., Van Dyk S. D., Jha S. W., Clubb K. I., Filippenko A. V., Mauerhan J. C., Miller A. A., Smith N., 2015, ApJ, 798, L37
Foley R. J., Jha S. W., Pan Y.-C., Zheng W. K., Bildsten L., Filippenko A. V., Kasen D., 2016, MNRAS, 461, 433
Freudling W., Romaniello M., Bramich D. M., Ballester P., Forchi V., García-Dabló C. E., Moehler S., Neeser M. J., 2013, A&A, 559, A96
Fruchter A. S. et al., 2006, Nature, 441, 463
Fynbo J. P. U. et al., 2006, Nature, 444, 1047
Gal-Yam A. et al., 2006, Nature, 444, 1053
Gal-Yam A., Maoz D., Guhathakurta P., Filippenko A. V., 2008, ApJ, 680, 550
Galbany L. et al., 2014, A&A, 572, A38
Galbany L. et al., 2016a, MNRAS, 455, 4087
Galbany L. et al., 2016b, A&A, 591, A48
Gehrels N. et al., 2006, Nature, 444, 1044
Gomes J. M. et al., 2016a, A&A, 585, A92
Gomes J. M. et al., 2016b, A&A, 588, A68
González Delgado R. M., Leitherer C., Heckman T. M., 1999, ApJS, 125, 489
Goobar A., 2017, Transient Name Server Classification Report, 762
Goudfrooij P., 1999, in Carral P., Cepa J., eds, ASP Conf. Ser. Vol. 163, Star Formation in Early Type Galaxies. Astron. Soc. Pac., San Francisco, p. 55
Hakobyan A. A., Mamon G. A., Petrosian A. R., Kunth D., Turatto M., 2009, A&A, 508, 1259
Hakobyan A. A., Adibekyan V. Z., Aramyan L. S., Petrosian A. R., Gomes J. M., Mamon G. A., Kunth D., Turatto M., 2012, A&A, 544, A81
Hakobyan A. A. et al., 2016, MNRAS, 456, 2848
Harmanen J. et al., 2015, Astron. Telegram, 8264
Howell D. A. et al., 2006, Nature, 443, 308
Hsiao E. Y. et al., 2013, Astron. Telegram, 5612
Izzo L. et al., 2017, preprint (arXiv:1704.05509)
James P. A., Anderson J. P., 2006, A&A, 453, 57
Jha S. W., 2017, preprint (arXiv:1707.01110)
Jha S., Branch D., Chornock R., Foley R. J., Li W., Swift B. J., Casebeer D., Filippenko A. V., 2006, AJ, 132, 189
Jha S. W. et al., 2013, Astron. Telegram, 5143
Jordan G. C., IV, Perets H. B., Fisher R. T., van Rossum D. R., 2012, ApJ, 761, L23
Kangas T. et al., 2017, A&A, 597, A92
Kasliwal M. M. et al., 2012, ApJ, 755, 161
Kauffmann G. et al., 2003, MNRAS, 346, 1055
Kennicutt R. C., Jr, 1998, ARA&A, 36, 189
Kewley L. J., Ellison S. L., 2008, ApJ, 681, 1183
Kewley L. J., Dopita M. A., Sutherland R. S., Heisler C. A., Trevena J., 2001, ApJ, 556, 121
Kewley L. J., Maier C., Yabe K., Ohta K., Akiyama M., Dopita M. A., Yuan T., 2013, ApJ, 774, L10
Kromer M. et al., 2013, MNRAS, 429, 2287
Kromer M. et al., 2015, MNRAS, 450, 3045
Krühler T., Kuncarayakti H., Schady P., Anderson J. P., Galbany L., Gensior J., 2017, A&A, 602, A85
Kuncarayakti H. et al., 2013a, AJ, 146, 30
Kuncarayakti H. et al., 2013b, AJ, 146, 31
Leibundgut B. et al., 1993, AJ, 105, 301
Leloudas G. et al., 2011, A&A, 530, A95
Leloudas G. et al., 2015, MNRAS, 449, 917
Li W. et al., 2003, PASP, 115, 453
Li W., Chornock R., Leaman J., Filippenko A. V., Poznanski D., Wang X., Ganeshalingam M., Mannucci F., 2011, MNRAS, 412, 1473
Liu Z.-W. et al., 2015a, MNRAS, 452, 838
Liu Z.-W., Moriya T. J., Stancliffe R. J., Wang B., 2015b, A&A, 574, A12
Liu Z.-W., Stancliffe R. J., Abate C., Wang B., 2015c, ApJ, 808, 138
Lunnan R. et al., 2014, ApJ, 787, 138
Lunnan R. et al., 2017, ApJ, 836, 60
Lyman J. D., James P. A., Perets H. B., Anderson J. P., Gal-Yam A., Mazzali P., Percival S. M., 2013, MNRAS, 434, 527
Lyman J. D., Levan A. J., James P. A., Angus C. R., Church R. P., Davies M. B., Tanvir N. R., 2016, MNRAS, 458, 1768
Lyman J. D. et al., 2017, MNRAS, 467, 1795
McClelland C. M. et al., 2010, ApJ, 720, 704
McCully C. et al., 2014a, Nature, 512, 54
McCully C. et al., 2014b, ApJ, 786, 134
Magee M. R. et al., 2016, A&A, 589, A89
Magee M. R. et al., 2017, A&A, 601, A62
Marino R. A. et al., 2013, A&A, 559, A114 (M13)
Meng X., Podsiadlowski P., 2014, ApJ, 789, L45
Michałowski M. J. et al., 2016, preprint (arXiv:1610.06928)
Modjaz M. et al., 2008, AJ, 135, 1136
Modjaz M., Kewley L., Bloom J. S., Filippenko A. V., Perley D., Silverman J. M., 2011, ApJ, 731, L4
Modjaz M. et al., 2014, AJ, 147, 99
Moriya T. J., Eldridge J. J., 2016, MNRAS, 461, 2155
Moriya T., Tominaga N., Tanaka M., Nomoto K., Sauer D. N., Mazzali P. A., Maeda K., Suzuki T., 2010, ApJ, 719, 1445
Narayan G. et al., 2011, ApJ, 731, L11
Ochner P., Tomasella L., Benetti S., Cappellaro E., Elias-Rosa N., Pastorello A., Turatto M., 2014, Astron. Telegram, 6648
Oey M. S., Parker J. S., Mikles V. J., Zhang X., 2003, AJ, 126, 2317
Osterbrock D. E., Ferland G. J., 2006, Astrophysics of gaseous nebulae and active galactic nuclei, 2nd edn. University Science Books, Mill Valley, CA
Pan Y.-C. et al., 2015, Astron. Telegram, 7534
Perets H. B. et al., 2010, Nature, 465, 322
Pettini M., Pagel B. E. J., 2004, MNRAS, 348, L59
Phillips M. M., 1993, ApJ, 413, L105
Phillips M. M., Wells L. A., Suntzeff N. B., Hamuy M., Leibundgut B., Kirshner R. P., Foltz C. B., 1992, AJ, 103, 1632
Phillips M. M. et al., 2007, PASP, 119, 360
Prieto J. L. et al., 2016, ApJ, 830, L32
Pumo M. L. et al., 2009, ApJ, 705, L138
Riess A. G. et al., 2016, ApJ, 826, 56
Ruiz-Lapuente P., Cappellaro E., Turatto M., Gouiffes C., Danziger I. J., della Valle M., Lucy L. B., 1992, ApJ, 387, L33
Sana H. et al., 2012, Science, 337, 444
Sánchez S. F. et al., 2012a, A&A, 538, A8
Sánchez S. F. et al., 2012b, A&A, 546, A2
Sánchez-Blázquez P. et al., 2006, MNRAS, 371, 703
Sanders N. E. et al., 2012, ApJ, 758, 132
Sarzi M. et al., 2006, MNRAS, 366, 1151
Sarzi M. et al., 2010, MNRAS, 402, 2187
Schlafly E. F., Finkbeiner D. P., 2011, ApJ, 737, 103
Shivvers I. et al., 2017, PASP, 129, 054201
Smette A. et al., 2015, A&A, 576, A77
Sofue Y., Rubin V., 2001, ARA&A, 39, 137
Soto K. T., Lilly S. J., Bacon R., Richard J., Conseil S., 2016, MNRAS, 458, 3210
Stanishev V., 2007, Astron. Nachr., 328, 948
Stanishev V., Rodrigues M., Mourão A., Flores H., 2012, A&A, 545, A58
Stanway E. R., Eldridge J. J., Greis S. M. L., Davies L. J. M., Wilkins S. M., Bremer M. N., 2014, MNRAS, 444, 3466
Stanway E. R., Eldridge J. J., Becker G. D., 2016, MNRAS, 456, 485
Stoll R., Prieto J. L., Stanek K. Z., Pogge R. W., 2013, ApJ, 773, 12
Stritzinger M., Mazzali P. A., Sollerman J., Benetti S., 2006, A&A, 460, 793
Stritzinger M. D. et al., 2014, A&A, 561, A146

Stritzinger M. D. et al., 2015, A&A, 573, A2
Svensson K. M., Levan A. J., Tanvir N. R., Fruchter A. S., Strolger L.-G., 2010, MNRAS, 405, 57
Taddia F. et al., 2013, A&A, 558, A143
Taddia F. et al., 2015a, A&A, 574, A60
Taddia F. et al., 2015b, A&A, 580, A131
Thöne C. C. et al., 2008, ApJ, 676, 1151
Tomasella L. et al., 2016, MNRAS, 459, 1018
Tonry J., Denneau L., Stalder B., Heinze A., Sherstyuk A., Rest A., Smith K. W., Smartt S. J., 2016, Astron. Telegram, 8680
Tripp R., 1998, A&A, 331, 815
Turatto M., Benetti S., Cappellaro E., Danziger I. J., Della Valle M., Gouiffes C., Mazzali P. A., Patat F., 1996, MNRAS, 283, 1
Valenti S. et al., 2009, Nature, 459, 674
van den Bergh S., Li W., Filippenko A. V., 2005, PASP, 117, 773
van Dokkum P. G., 2001, PASP, 113, 1420
Vulcani B. et al., 2014, MNRAS, 441, 1340
Wang B., Justham S., Han Z., 2013, A&A, 559, A94
Wang B., Meng X., Liu D.-D., Liu Z.-W., Han Z., 2014, ApJ, 794, L28
White C. J. et al., 2015, ApJ, 799, 52
Xiao L., Eldridge J. J., Stanway E., Galbany L., 2017, preprint (arXiv:1705.03606)
Zapartas E. et al., 2017, A&A, 601, A29

APPENDIX A: THE LATE-TIME SPECTRA OF SNE 2015H AND 2014DT

Our MUSE observations included a significant time lag in order to analyse the underlying galaxy light at the explosions sites. Nevertheless, for SNe 2014dt and 2015H we were able to detect prominent forbidden emission that is associated with SNe Iax at late phases. Although a full analysis of the SN signal is beyond the scope of this work, we present their spectra for completeness and compare to the comprehensive analysis of late-time SN Iax spectra sample by Foley et al. (2016). For this, we extracted flux in spaxels centred on the SN emission within a radius equal to the seeing of the image.

Our SN 2014dt spectrum is at a phase of approximately +450 rest-frame days post-maximum, which makes it the latest spectrum of an SN Iax to our knowledge. In Fig. A1, we compare our spectrum in a region of strong forbidden line emission to those of Foley et al. (2016), which were taken at +270 and +410d. As those authors noted based on their +410 d spectrum (to which our +450 d spectrum is almost identical), there is a general lack of evolution between these epochs in line strength or widths. Our SN 2014dt observations were taken under challenging sky conditions and the regions of interest are affected by residual sky emission not removed by the MUSE data reduction (Section 2.1) – for the sake of presentation of Fig. A1 we have manually subtracted the signal from a very faint region of the data cube.

The early spectra and light curve of SN 2015H were analysed by Magee et al. (2016) and our MUSE observation adds a late-time spectrum at an epoch of +291 d post-maximum. SNe Iax display a wide range of morphologies in their spectra around these wavelengths at similar epochs, as shown in fig. 8 of Foley et al. (2016) and we note a very strong similarity between SN 2002cx and SN 2015H. As with SN 2014dt, we present a region of strong forbidden line emission in Fig. A2 where we also plot the best-fitting 10-parameter model of Foley et al. (2016) in order to compare more quantitatively with SN 2002cx. As with SN 2002cx, we see that [Ni II] λ7378 emission is dominated by its broad component (FWHM ~ 8000 km s^{-1}, cf. 7870 km s^{-1} for SN 2002cx), with the narrow components of [Fe II] λ7155 and [Ca II] λ7291,7324 being more prominent, albeit somewhat narrower (FWHM ~ 800 km s^{-1} cf. 1430 km s^{-1} for SN 2002cx).

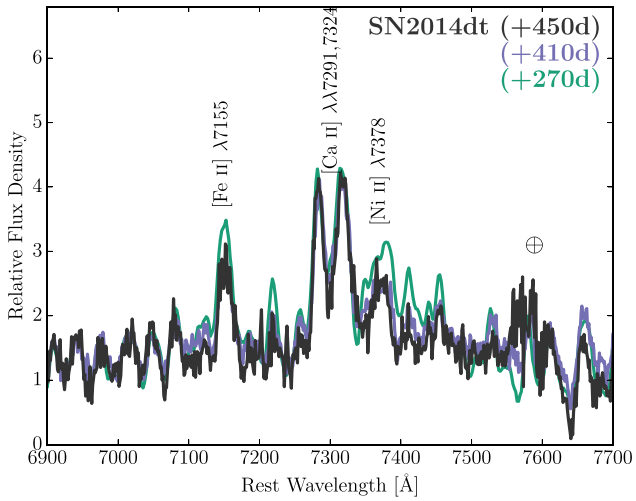

Figure A1. The late-time spectrum of SN 2014dt extracted from the MUSE data cube at an epoch of ∼+450 d after maximum, centred around prominent forbidden lines. Also shown are the +270 and +410 d spectra of Foley et al. (2016), we confirm a general lack of evolution in the strength or widths of the forbidden lines between the +270d spectra, although the [Ni II] λ7378 flux is slightly depressed. Our spectrum shows very little evolution from the +410d spectrum, with only perhaps a slight weakening of the ∼7670 Å feature.

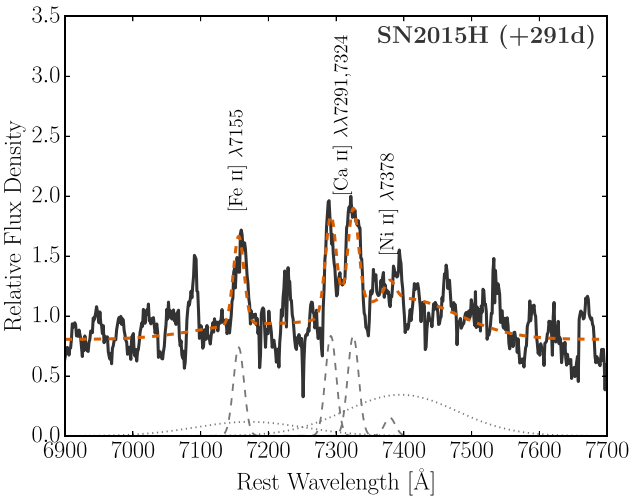

Figure A2. As for Fig. A1 but here showing SN 2015H at an epoch of +291 d. The 10 component model, following the methodology of Foley et al. (2016) is shown. The morphology and line kinematics of the spectrum are similar to those of SN 2002cx at a similar epoch.

We additionally note that we do not expect emission from these SNe that would affect our main environmental analysis, in the absence of circumstellar interaction, of which there appears to be no evidence. When running these SN spaxel bins as part of our main fitting procedure, STARLIGHT masked over the SNe features (such as those shown in Figs A1 and A2) as part of a sigma clipping routine. We found that manually masking large regions of the input spectra that may be affected by SN emission made very little difference to our emission line results. Late in the manuscript's preparation, we were able to check the effect of the SN emission for SN 2015H

Table B1. Emission line fluxes at the explosion sites of SNe Iax, corrected for Galactic extinction. Line strengths are given relative to the Hα flux, F(Hα). For the NOT sample, [S II] are given as the sum of the lines λ6716 + λ6731.

SN	F(Hα) ($\times 10^{-16}$ erg s^{-1})	H β	[O III]		[N II]		[S II]	
			λ4959	λ5007	λ6548	λ6583	λ6716	λ6731
				MUSE sample				
1991bj	21.59	0.278	0.100	0.309	0.064	0.184	0.224	0.159
2002bp	0.15	–	–	–	–	1.136	–	–
2002cx	9.05	0.301	0.113	0.355	0.066	0.188	0.231	0.177
2004cs	27.00	0.290	0.078	0.218	0.083	0.254	0.231	0.172
2005P	1.73	0.252	–	0.264	0.044	0.163	0.301	0.202
2005hk	0.51	0.290	–	0.248	0.059	0.112	0.313	0.204
2008ae	3.78	0.287	0.060	0.168	0.118	0.392	0.235	0.166
2008ha	32.13	0.439	0.376	0.990	0.026	0.079	0.167	0.119
2009J	7.72	0.284	0.124	0.339	0.102	0.323	0.258	0.185
2010ae	378.23	0.280	0.169	0.493	0.058	0.177	0.216	0.150
2010el	24.57	0.202	0.070	0.169	0.202	0.595	0.263	0.181
2011ce	249.84	0.245	0.020	0.052	0.127	0.378	0.179	0.129
2012Z	4.81	0.316	0.110	0.267	0.086	0.231	0.300	0.207
2013gr	4.08	0.310	0.195	0.547	0.035	0.106	0.300	0.202
2014dt	42.74	0.234	0.045	0.144	0.168	0.539	0.237	0.158
2014ey	1.75	0.261	0.085	0.203	0.078	0.258	0.271	0.197
2015H	2.95	0.144	–	0.084	0.072	0.411	0.277	0.143
				NOT sample				
2003gq	38.99	0.158	–	–	–	0.126	0.132	
2005cc	55.52	0.135	–	–	–	0.302	0.204	
2006hn	15.69	0.309	–	0.170	–	0.398	0.282	
2007J	38.60	0.288	–	0.288	–	0.200	0.295	
2009ku[a]	17.82	0.282	–	0.363	–	0.219	0.316	
2013dh	37.82	0.324	–	0.069	–	0.372	0.282	
2013en	44.03	0.295	–	–	–	0.251	0.331	
2014ek	60.88	0.209	–	–	–	0.295	–	
PS 15csd[b]	8.56	0.295	–	0.525	–	0.112	0.363	

Note. [a]SN overlaid on a small, unresolved host.

as MUSE re-observed the SN location. Although the observations were aborted due to scheduling restrictions, 2 × 700 s exposures were taken. We measured metallicities at the SN location on the first exposure (as the second was of poorer quality). Our values of 8.67 ± 0.10 and 8.56 ± 0.03 dex agree excellently with the values from our original observations of 8.66 ± 0.07 and 8.56 ± 0.03 dex for D16 and M13 (N2), respectively.

With these results, we highlight the power of MUSE as an extremely efficient optical spectrograph to obtain nebular phase spectra of SNe, whilst obtaining spectral information at the explosion site and across the host for free, providing legacy value to the data for a wealth of galactic studies not possible with traditional long-slit spectroscopy.

APPENDIX B: EXPLOSION-SITE LINE FLUXES

In Table B1, we provide individual flux measurements for the SN Iax explosion sites. These values have been corrected for Galactic reddening but not local reddening, i.e. before our Balmer decrement correction.

APPENDIX C: METALLICITY MAPS

In Fig. C1, we show stamps of D16 metallicity maps for the MUSE sample of SNe Iax hosts, excluding SN 2008ge, which is discussed and shown in Section 6.3.

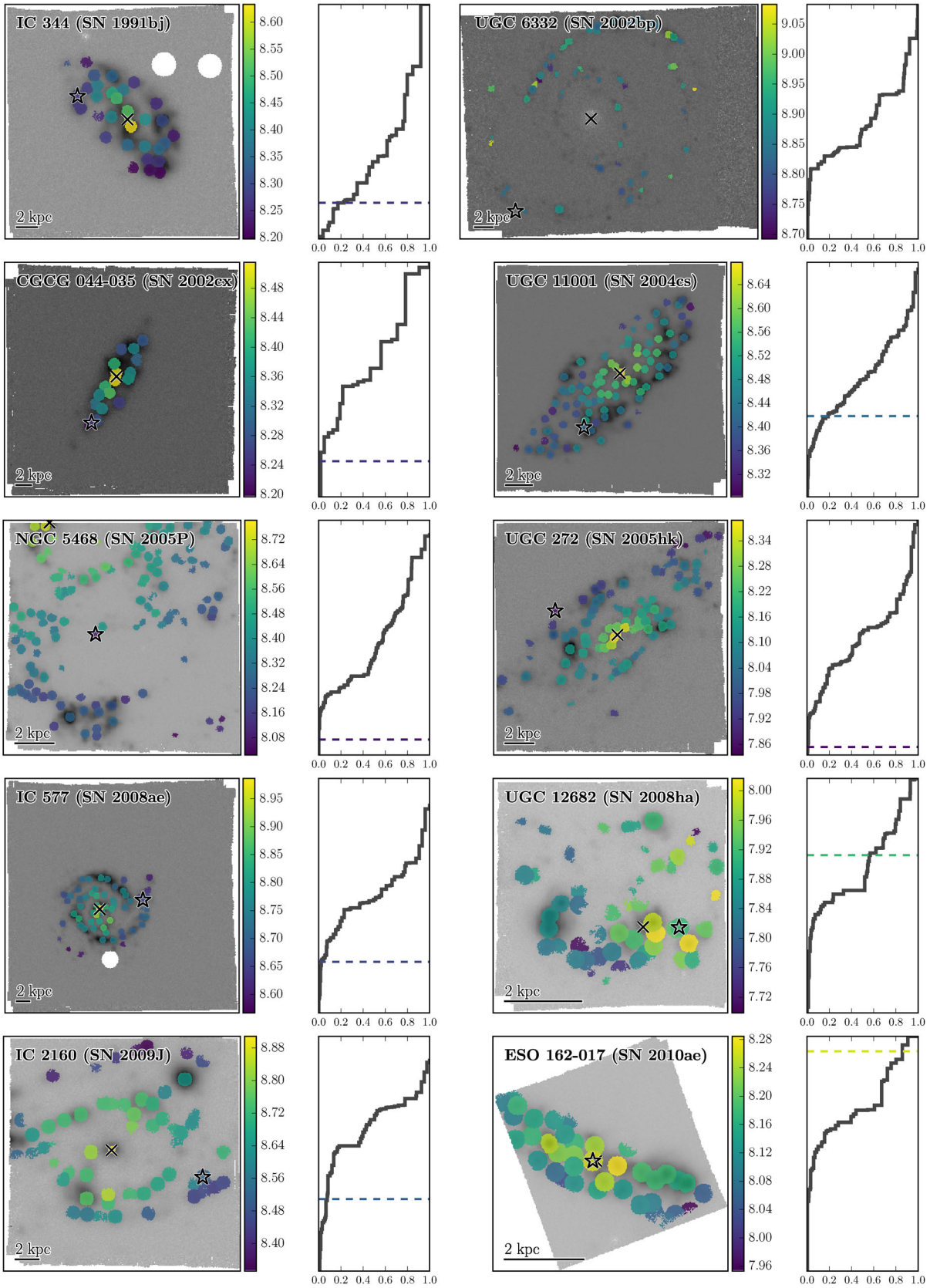

Figure C1. The metallicity maps of SNe Iax host galaxies using the indicator of D16 (see Section 3.3.2). Host nuclei and the SN explosion-site positions are given by black × and 'star' symbols, respectively. To the right of each map, the cumulative fraction of SF (abscissa) with metallicity is given (following Fig. 3, top right panel). The SN location indicated by the dashed line (except for SN 2002bp where we rely on a metallicity gradient estimate for the SN environment of $Z = 8.88$ dex). The vertical axis of the cumulative plots matches the colour bar for the corresponding metallicity map. North is up, east is left.

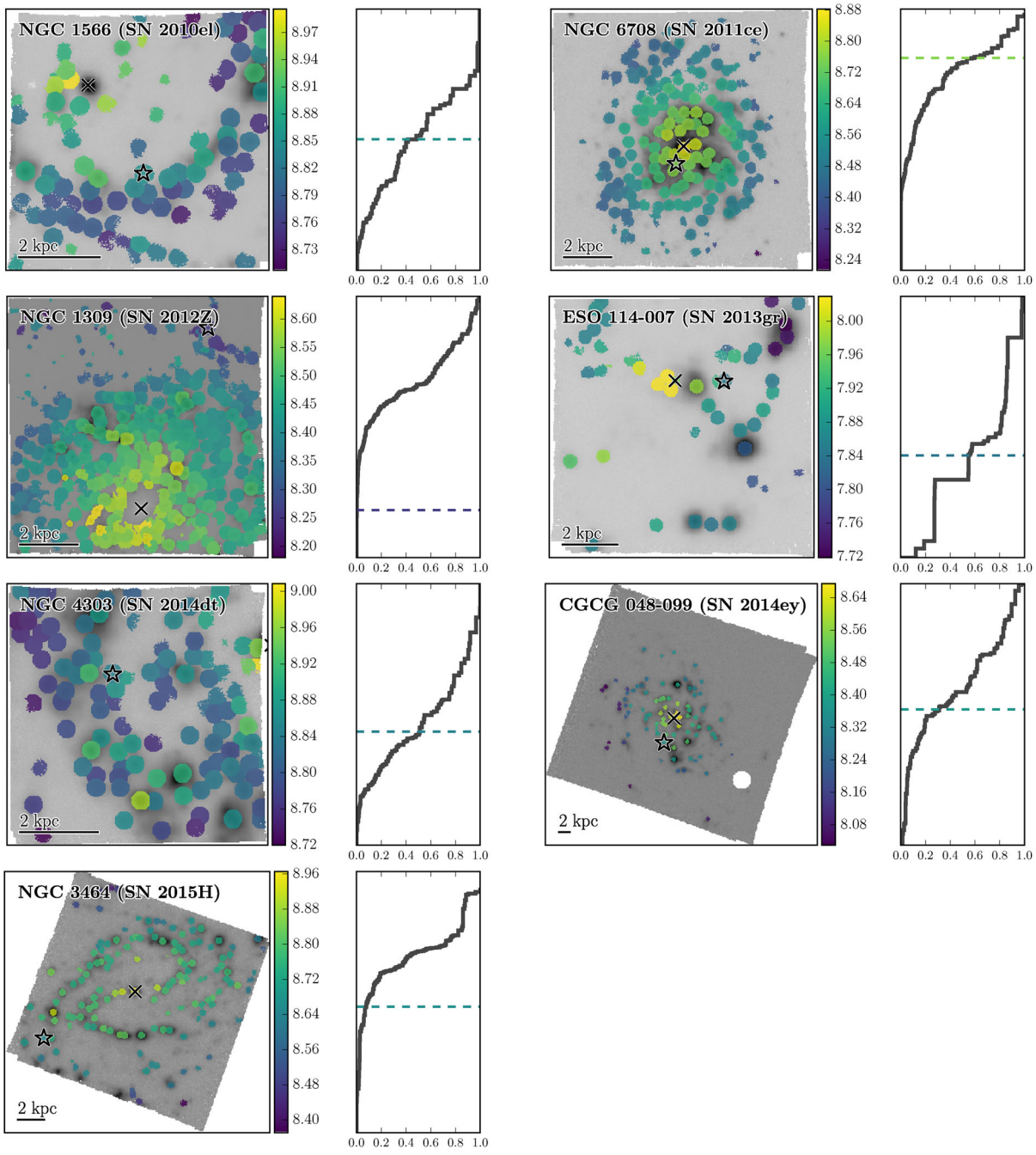

Figure C1 – *continued*

This paper has been typeset from a TEX/LATEX file prepared by the author.